MID-AMERICA TRANSPORTATION CENTER

UNIVERSITY OF Nebraska Lincoln

THE UNIVERSITY OF IOWA

KU THE UNIVERSITY OF KANSAS

MISSOURI S&T

LINCOLN UNIVERSITY MISSOURI

NICC NEBRASKA INDIAN COMMUNITY COLLEGE

UNIVERSITY OF Nebraska Omaha

University of Nebraska Medical Center

KU MEDICAL CENTER The University of Kansas

Shallow River Ice Flow Impacts on Critical Infrastructure

Richard L Wood, PhD
Associate Professor
Department of Civil and Environmental Engineering
University of Nebraska-Lincoln

David Admiraal, PhD
Associate Professor

Tirthankar Roy, PhD
Assistant Professor

Gul Ahmad Laiwal
Graduate Student Researcher

Mitra Nasimi
PhD Candidate
Graduate Student Researcher

Sudan Pokharel
Graduate Student Researcher

UNIVERSITY OF Nebraska Lincoln

2024

A Cooperative Research Project sponsored by U.S. Department of Transportation- Office of the Assistant Secretary for Research and Technology

MATC

Shallow River Ice Flow Impacts on Critical Infrastructure

Richard L. Wood, Ph.D.
Associate Professor
Department of Civil and Environmental
Engineering
University of Nebraska-Lincoln

David Admiraal, Ph.D.
Associate Professor
Department of Civil and Environmental
Engineering
University of Nebraska-Lincoln

Tirthankar Roy, Ph.D.
Assistant Professor
Department of Civil and Environmental
Engineering
University of Nebraska-Lincoln

Gul Ahmad Laiwal
Graduate Student Researcher
Department of Civil and Environmental
Engineering
University of Nebraska-Lincoln

Mitra Nasimi
Ph.D. Candidate/Grad. Student Researcher
Department of Civil and Environmental
Engineering
University of Nebraska-Lincoln

Sudan Pokharel
Graduate Student Researcher
Department of Civil and Environmental
Engineering
University of Nebraska-Lincoln

Technical Report Documentation Page

1. Report No. 25-1121-0005-004-58	2. Government Accession No.	3. Recipient's Catalog No.	
4. Title and Subtitle Shallow River Ice Flow Impacts on Critical Infrastructure		5. Report Date September 2024	
		6. Performing Organization Code	
7. Author(s) Richard L. Wood, https://orcid.org/0000-0002-8642-2217 David Admiraal, https://orcid.org/0000-0002-6654-3740 Tirthankar Roy, https://orcid.org/0000-0002-6279-8447 Gul Ahmad Laiwal, none Mitra Nasimi, https://orcid.org/0000-0003-2364-0118 Sudan Pokharel, https://orcid.org/0009-0009-7010-698X		8. Performing Organization Report No. 25-1121-0005-004-58	
9. Performing Organization Name and Address Mid-America Transportation Center Prem S. Paul Research Center at Whittier School 2200 Vine St. Lincoln, NE 68583-0851		10. Work Unit No. (TRAIS)	
		11. Contract or Grant No. 69A3551747107	
12. Sponsoring Agency Name and Address Office of the Assistant Secretary for Research and Technology 1200 New Jersey Ave., SE Washington, D.C. 20590		13. Type of Report and Period Covered November 2021 - June 2023	
		14. Sponsoring Agency Code MATC TRB RiP No. 91994-107	
15. Supplementary Notes			

16. Abstract

This research investigates ice jams and ice flows in Nebraska rivers, which are distinct from those in other regions due to the unique fluvial geomorphology of these rivers, characterized by high sediment loads, steep gradients, and wide, braided channels. The study aims to develop a two-dimensional hydrodynamic model to predict ice jam behavior using data from uncrewed aerial system surveys of several Nebraska rivers, including the Loup and Niobrara Rivers. This model integrates platforms such as HEC-RAS 2D and QGIS with a modified Shallow Water Equation to simulate ice effects. Preliminary results indicate that ice flows significantly alter river morphology, affecting floodplain characteristics and damaging infrastructure. The research encompasses detailed site selection, data collection, and analysis of ice thickness and roughness, providing essential data for hydraulic modeling. This work not only advances the understanding of ice jams in unique geomorphological settings but also supports the design of infrastructure resilient to ice-related hazards in these regions.

17. Key Words Ice Jams, UAS, river monitoring, hydraulic modeling		18. Distribution Statement	
19. Security Classif. (of this report) Unclassified	20. Security Classif. (of this page) Unclassified	21. No. of Pages 85	22. Price

Table of Contents

List of Figures

List of Abbreviations

Comprehensive River Ice Simulation System Project (CRISSP)

Digital elevation model (DEM)

Hydrologic Engineering Centre's River Analysis System (HEC-RAS)

Light detection and ranging (lidar)

Mid-America Transportation Center (MATC)

Nebraska Transportation Center (NTC)

one-dimensional (1D)

shallow water equation (SWE)

Structure-from-Motion (SfM)

three-dimensional (3D)

two-dimensional (2D)

uncrewed aerial systems (UASs)

Disclaimer

The contents of this report reflect the views of the authors, who are responsible for the facts and the accuracy of the information presented herein. This document is disseminated in the interest of information exchange. The report is funded, partially or entirely, by a grant from the U.S. Department of Transportation's University Transportation Centers Program. However, the U.S. Government assumes no liability for the contents or use thereof.

Abstract

This research investigates ice jams and ice flows in Nebraska rivers, which are distinct from those in other regions due to the unique fluvial geomorphology of these rivers, characterized by high sediment loads, steep gradients, and wide, braided channels. The study aims to develop a two-dimensional hydrodynamic model to predict ice jam behavior using data from uncrewed aerial system surveys of several Nebraska rivers, including the Loup and Niobrara Rivers. This model integrates platforms such as HEC-RAS 2D and QGIS with a modified Shallow Water Equation to simulate ice effects. Preliminary results indicate that ice flows significantly alter river morphology, affecting floodplain characteristics and damaging infrastructure. The research encompasses detailed site selection, data collection, and analysis of ice thickness and roughness, providing essential data for hydraulic modeling. This work not only advances the understanding of ice jams in unique geomorphological settings but also supports the design of infrastructure resilient to ice-related hazards in these regions.

Chapter 1 Overview and Project Outline

1.1 Overview of Project

This study recognizes that ice jams and ice flows in many Nebraska rivers differ significantly from those in other regions. Nebraska experiences remarkable impacts from ice, largely due to the unique fluvial geomorphology of many of its rivers. These rivers, located at the southern end of the normal range of ice-impacted rivers, are characterized by high sediment loads and wide conveyance areas. The high sand loads result in relatively steep river gradients compared to those in other parts of North America, leading to braided or multi-channel formations. Although these rivers are generally wide, the majority of the conveyance area is active only part of the year. Finally, many of these rivers are very shallow, leading to rapid formation of large quantities of ice during cold weather.

However, these rivers are not uniform. For instance, the Niobrara River has a wide conveyance area, but the floodplain is relatively narrow in the studied areas due to surrounding bluffs. In contrast, the Loup River features a relatively wide floodplain in the studied regions. Observations were also made on the Missouri River, which has a relatively deep cross-section due to channelization. Much of the floodplain here is restricted from flow by levees, and flow is primarily influenced by controlled releases upstream. The formation of ice jams and ice flows in these rivers can vary considerably. Understanding how ice jams and river ice impact infrastructure is crucial for informing future engineering infrastructure designs.

1.2 Research Objectives

This research project, as described in this report, had three primary objectives. The first objective is to measure the geometries and dynamic behavior of deposited ice and ice flows. These measurements include the geometries of deposited ice—such as shape, size, thickness, and

embedment angle—along with flow velocities, the rotation of drift ice, and other properties of ice jams and ice flows. The second objective is to map the spatial distributions of ice jams and ice flows in regions where ice is recognized as a hazard. The third and final objective is to model the dynamics of ice flows and ice jam formation using a hydraulics model calibrated to incorporate the effects of floating ice and shallow water.

1.3 Research Tasks and Overview

The research was originally divided into five tasks described below. For additional details on each chapter, refer to the next section for the outline of the report and its structure.

1.3.1 Task 1: Literature Review and 2D-Hydrodynamic Model Selection

Numerous ice jam models with varying degrees of complexity have been developed, with most being one-dimensional (Manitoba Hydro, 2022). The first task of this project was to select the hydraulics/ice jam model(s) most suitable for shallow water ice flows and ice jams in two dimensions. Several models were identified, including CRISSP 2D and HEC-RAS. The main issue with CRISSP 2D was obtaining access to the program. Currently owned by Manitoba Hydro, the program required a lengthy licensure process, and although the team eventually secured a copy, they were unable to get the basic executable to run. Additionally, CRISSP 2D requires the use of SMS (Surface Modeling Software), a proprietary program for developing the 2D finite element mesh, with results viewable in TECPLOT, another proprietary program.

HEC-RAS, on the other hand, is primarily designed to model ice flows in one dimension, with the assumption that bank anchoring is the primary mechanism by which ice jams are held in place. However, HEC-RAS 2D offers sophisticated flow modeling capabilities that can simulate a wide range of flow conditions. Although ice flow and ice jam modeling are not built-in features of HEC-RAS 2D, it may be possible to model them using the program's advanced API or if

Manning's roughness is used as a surrogate of ice flow resistance. This approach was adopted, primarily due to the limited accessibility of CRISSP 2D throughout the project's duration.

1.3.2 Task 2: Site Selection and Collection of Aerial Data

A UAS (uncrewed aerial system) was employed to collect geographic data, including information on ice jams and ice flows, at five sites in Nebraska: (1) the Missouri River near Omaha, (2) the Loup River near Columbus, (3) the North Loup River at St. Paul, (4) the Niobrara River at the Highway 11 crossing, and (5) the Niobrara River at the Highway 281 crossing. These sites were selected due to their documented history of ice jams and their susceptibility to future jams and ice flows. The aerial data collected at these locations included extensive surveys of ice jam spatial distributions, ice slab dimensions, and concurrent ice flows. The ice flow information was used to assess river flow patterns. Aerial data were gathered during the summer for topographic purposes and during the spring ice breakup to observe planform adjustments in flow patterns caused by river ice. Real-time reporting of existing ice jams by the Nebraska Department of Natural Resources and the U.S. Army Corps of Engineers assisted in site selection.

1.3.3 Task 3: Collection of Meteorological and Hydrological Data

As part of the project, detailed flow data were collected from gauging stations near the study sites. The most valuable data included streamflow measurements, which were organized into LP3 plots to understand recurrence intervals. Typically, ice breaks occur in March, with the most severe ice flow events associated with large storm flows. Bathymetric data were collected at three sites—the Loup River near Columbus and the two Niobrara sites. These bathymetric data were instrumental in complementing the information gathered through the UAS system.

1.3.4 Task 4: 2D-Hydrodynamic Model and Analysis Validation

Using HEC-RAS 2D, two-dimensional flow models were developed for the Loup River near Columbus and the two Niobrara River sites. Data collected using the UAS, along with hand measurements and lidar data available from the U.S. Geological Survey (USGS, 2022), were used to develop these models.

1.3.5 Task 5: Documentation of Procedures

Information about data collection and modeling was developed as part of this work and is reported herein to enhance the efficiency of future studies.

1.4 Report Organization

This report is divided into six chapters. Chapter 2 provides background information, including a literature review on ice jams and their characteristics. Chapter 3 presents the site selection process and the field data collected using an uncrewed aerial system (UAS), along with its respective processing. Chapter 4 summarizes the characteristics of the physical properties derived from the UAS data. Chapter 5 outlines the hydraulic model within HEC-RAS and details its methodology. Finally, the conclusions of the project are presented in Chapter 6.

Chapter 2 Background

<u>2.1 Overview on Ice Jams</u>

River ice cover forms in cold regions with freezing temperatures such as the Nelson

River in Canada, Mississippi River in the United States, and Kanas Lake in China. Ice covers in

rivers affect the economy of a society when floods caused by ice jams pose threats to hydraulic

infrastructure and inland waterways. High floods occur during the spring season due to melting

and breaking of ice-covered layers in rivers (Wang et al., 2021)

2.1.1 Ice Jam Formation

Open water and partial ice cover forms a turbulent flow field. Partial and full ice cover,

unlike open water, affects the flow over the entire cross section of the river. Sukhodolov et al.

(1999) found that the turbulent flow in ice covered rivers becomes more complicated than open

channel flow. The availability of data beneath the ice layer is also difficult to collect in the field.

It is difficult and dangerous to collect data beneath the ice layer in the field, therefore flow

beneath ice covers are not as widely studied as open water flow (Nyantekyi-Kwakye et al.,

2019).

An ice jam induced backwater level is higher than one that results from an intact floating

ice cover or in open channel flow. Compared to open channel flow, ice jams result in flow depths

2-3 times higher for an equivalent or a smaller discharge. Therefore, it becomes very complex

and difficult to predict the magnitude of ice jam flooding (Rokaya et al., 2022).

Border ice forms in slow-moving water. In calm water vertical mixing is reduced, the

projecting bed material forms the thermal surface ice and continues to grow, moving laterally

where turbulent flow stops its progression (Bergeron et al., 2011). When ice formation stops, the

ice growth results in partial ice cover (PIC). Flow data under partial ice cover is difficult to

collect due to the low strength of thin ice. Sometimes the entire river is fully covered with ice depending on the hydraulic and meteorological conditions (Nyantekyi-Kwakye et al., 2021).

2.1.2 Consolidation of River Ice Processes

Frazil ice forms in sections of the river with turbulent flows of coarse-grained riffles. Frazil crystals form in the turbulent cooled water of rapids and rifles. The surface of the water is supercooled and with no static ice layer, heat is lost from the surface. Frazil crystal formation is followed by frazil grouping together and formation of flocs. Flocs tend to move to the surface and underneath the ice surface because of their buoyancy. Pan shape structures called pans form after flocs freeze together and finally rafts are formed from pans. Constrictions are caused by meander bends, bridge piers, and border ice progression causing ice bridging. Frazil ice pans and rafts can freeze together to form frazil ice jams (Bergeron et al., 2011).

Anchor ice forms on streambeds in supercooled turbulent flow. Anchor ice accumulation is difficult to study; unlike frazil ice and border ice, anchor ice occurs at temperatures close to the melting point of water. Anchor ice increases the stage of the stream, thus decreasing the discharge (Nafziger et al., 2017). Thick anchor ice often blocks frazil ice pans, creating a dam in the form of a stationary ice front and resulting in a solid ice cover upstream of the anchor ice dam (Bergeron et al., 2011).

2.2 Characteristics of Jams and Implications for Infrastructure

According to Hicks and Beltaos (2008), there are two types of ice breakups: the spring breakup, and mid-winter thaws. The main difference between these two types of breakups is the ice condition at the time of breakup. Spring breakups are characterized by warming temperatures and low river flows, whereas mid-winter thaws are forced by hydrologic events, such as rain-on-snow events, which occur while cold conditions persist. The mid-winter thaws cause the most

damage, as the ice retains most of its strength and is only dislodged by rising flow conditions. In northern climates, mid-winter thaws may be followed by freeze-ups that affix flooded ice jams in place for longer periods. Perhaps the best way to distinguish these two types of events is that one is forced by gradual increases in temperature, whereas the other is forced by rapid introduction of flow.

In Nebraska, the mid-winter thaw type of ice flow is mostly caused by rain-on-snow or rain-on-frozen ground. In most Nebraska cases, the term mid-winter thaw might not be appropriate, because the winters in Nebraska are shorter than farther north, where the terminology developed. In Nebraska, two main things are needed to force severe ice-jams: (1) a cold winter period, followed by (2) a rapid breakup of the ice (usually due to excess rainfall). These two things generally only culminate in late February to early March. This is exactly what happened in 2019 when ice runs were observed across the entire eastern side of the state. While such an event could be followed by a refreeze, it is much less likely than in northern areas. In any case, such events are not common, but neither are they uncommon. Instead, significant ice jams happen periodically, depending on weather conditions from December to March.

Hicks and Beltaos (2008) point out that one of the primary goals of ice jam studies is to determine stages. The example they use is that of a bridge deck, which must be high enough to avoid damage from ice jams. They also suggest two methods for predicting what that height must be—empirical, based on historic records of ice jam depths, and analytical.

2.3 UAS Overview and Introduction

It is also difficult to perform direct measurements on ice flow in rivers and on surface ice of glaciers because only rivers and a few glaciers have automatic weather stations in North America. However, recent development in uncrewed aerial systems (UASs) allow high

resolution photogrammetry which produces very detailed detection of ice covers (Bash & Moorman, 2020).

UASs have been used with high resolution cameras to obtain data for ice river topography. Compared to traditional aerial systems, this type of system is cost effective and easy to use for survey processes. Also, there is less risk involved with UAS surveys compared to conventional surveys. Currently the common practice has been to use Structure-from-Motion (SfM) to obtain a three-dimensional model of the ice surface from the two-dimensional images captured by UASs (Ehrman et al., 2021).

The use of UASs for ice cover surface surveys offers several advantages over other survey methods, such as ground-based measurements or satellite imagery. First, UASs can fly at low altitudes, providing a higher resolution than satellite images. Second, they can cover large areas quickly, making it possible to survey entire river systems in a short time, allowing the surveyors to safely survey ice cover rivers without the need to walk the river as in traditional surveys. Finally, UASs enable researchers to collect data in real-time. The changes in ice cover as they occur can be monitored, allowing for more accurate and timely assessments of ice dynamics.

Using uncrewed aerial systems (UASs) with high resolution (SfM) is practical for surveys on large-sized rivers, medium-sized rivers, and small streams covered in ice. The data from UASs provide useful information on ice break-up processes, which is important for predicting the time of ice jam formation because ice jams pose risks to critical infrastructure such as bridges, small-size dams, and highways (Alfredsen et al., 2018).

<u>2.4 Existing Computer Models</u>

Many ice jam models have been developed. There are some two-dimensional models, but most models are one-dimensional. The first is CRISSP, Comprehensive River Ice Simulation System Project, on which development began in 2000. CRISSP2D is a two-dimensional hydrodynamic numerical model developed from DynaRICE and RICEN models. The current CRISSP2D model performs both freeze-up and breakup ice jam processes and allows for the analysis of both unsteady and transitional flow conditions. For instance, the CRISSP 2D model analyzes frazil ice production, border ice development and thermal growth of ice covers, and surface ice (Wazney et al., 2015).

The second ice jam model is RIVICE. RIVICE is a one-dimensional hydrodynamic model that uses numerical methods to simulate ice jams. RIVICE models the ice jam with time steps from minutes to seconds to simulate rapid events with available meteorological and bathymetric parameters (Rokaya et al., 2019). However, the RIVICE ice jam model cannot model ice jams in two dimensions.

The third is HEC-RAS and it is a very commonly utilized hydraulic program. Hydrologic Engineering Centre's River Analysis System (HEC-RAS) is convenient for open-water flow, ice-cover flow, ice jams, and a combination of any of these (Beltaos et al., 2012). HEC-RAS removes the slope corrections from the SWE and sets the non-Newtonian stress to zero. Therefore, HEC-RAS simplifies the SWE equation to the so called clear-water equation.

HEC-RAS can model ice jams in one dimension; it can also model open water flow using a simpler form of SWE called the clear-water equation, however, HEC-RAS cannot model ice flow in two dimensions. River ice transport and ice run processes have two-dimensional properties due to irregular geometries of the channel, friction of riverbanks and the non-

uniformity of the water content. Ice flow may be modeled only with limited applicability in one dimension (Shen et al., 2000).

A simplified 2D Shallow Water Equation (SWE) is used in HEC-RAS 2D modeling of open channel flow. HEC-RAS does not include the necessary parameters for a two-dimensional ice jam flow. SWE cannot account for the length of ice jams, the Manning's roughness coefficient of the undersurface of ice cover, change in the flow area and the beginning time of the ice jam, and break of the ice jams (Krylenko et al., 2020).

2.5 Modified Shallow Water Equations (SWE)

The shallow water equations (SWE) are used to approximately calculate the two-dimensional flow of water or any other liquid. The basic assumption in SWE is that the lateral velocities are depth-averaged, and the vertical component of the velocity is neglected assuming only horizontal water velocities (Hergarten & Robl, 2015). In vector notation, the SWE are given as:

$$\frac{\partial}{\partial t} v_h + (v_h.\nabla)v_h = gs - \frac{\tau}{\rho h_v} \frac{v_h}{|v_h|} \tag{2.1}$$

The continuity equation is given by

$$\frac{\partial}{\partial t} h_v + div(h_v.v_h) = 0 \tag{2.2}$$

Hergarten & Robl (2015) combined the shallow water equation with the equation of continuity and applied three modifications to the combined equation. First, the real acceleration that acts in the same direction as the surface of the flow is corrected by multiplying it with a vertical slope correction factor in the vertical direction. Second, the friction term is corrected by applying a smaller factor than for the vertical acceleration because the angle corresponding to the

acceleration is smaller and the slope correctors in the vertical directions are applied by the taking the cosines of the angles. Finally, the vertical depth of flow is corrected by applying the slope correction factor, which is the same as that used for acceleration. The final equation is given by:

$$
\begin{aligned}
\frac{\partial}{\partial t}(h_v v_h) + div\left(h_v v_h v_h^T + \frac{1}{2} g h_v^2 I\right) \\
= -g h_v \nabla_{zb} - f(h_v, v_h, \varphi, \psi) h_v v_h
\end{aligned}
\tag{2.3}
$$

HEC-RAS removes the slope corrections from the SWE and sets the non-Newtonian stress to zero. Therefore, HEC-RAS simplified the SWE to the clear-water equation. The 2D depth-integrated hydrodynamic equation for shallow water flow that includes ice effects is given by (Shen et al., 2000):

$$
\frac{\partial H}{\partial t} + \frac{\partial q_x}{\partial x} + \frac{\partial q_y}{\partial y} = \frac{\partial(N_i t^s)}{\partial t}
\tag{2.5}
$$

$$
\begin{aligned}
\frac{\partial q_x}{\partial t} + \frac{\partial}{\partial x}\left(\frac{q_x^2}{H_p}\right) + \frac{\partial}{\partial y}\left(\frac{q_x q_y}{H_p}\right) \\
= -\frac{1}{\rho_w}(\tau_{bx} - \tau_{ix}) - g H_p \frac{\partial \eta}{\partial x} + \frac{1}{\rho_0}\left(\frac{\partial T_{xx}}{\partial x} + \frac{\partial T_{yx}}{\partial y}\right)
\end{aligned}
\tag{2.6}
$$

$$
\begin{aligned}
\frac{\partial q_y}{\partial t} + \frac{\partial}{\partial x}\left(\frac{q_x q_y}{H_p}\right) + \frac{\partial}{\partial x}\left(\frac{q_y^2}{H_p}\right) \\
= -\frac{1}{\rho_w}(\tau_{by} - \tau_{iy}) - g H_p \frac{\partial \eta}{\partial y} + \frac{1}{\rho_0}\left(\frac{\partial T_{xy}}{\partial x} + \frac{\partial T_{yy}}{\partial y}\right)
\end{aligned}
\tag{2.7}
$$

In this equation, t is the time and x, y are the space variables. H is the water depth and H_p is the water depth below the ice cover layer. η is the elevation of water surface. q_x and q_y are the unit discharge in the x and y directions. N_i is the concentration of ice and t^s is the thickness of

the submerged accumulated ice. ρ_0 is the water density. τ_b and τ_i are the shear stresses at the riverbed and at the interface of water and ice, respectively.

$$T_{ij} = \varepsilon_{ij}^w \left(\frac{\partial q_i}{\partial x_j} + \frac{\partial q_j}{\partial x_i} \right) \tag{2.8}$$

ε_{ij}^w is the eddy viscosity coefficient and i and j show the coordinates in the x and y directions. T_{ij} can be rewritten more simply as

$$T_{ij} = \frac{1}{H} \int_{zb}^{zh} \{viscous + turbulent + differential\ advection\}\ dz \tag{2.9}$$

In 3-D modeling, viscous and turbulent stresses are often modeled separately, and the most common type of model used for the turbulent stresses is a two-equation eddy viscosity model. For depth-averaged flows, there are the additional differential advection terms, so viscous, turbulent, and differential advective terms are often lumped together and modeled using a pseudo viscosity (v_t) term.

$$T_{ij} = v_t \frac{\partial U_i}{\partial x_j} \tag{2.10}$$

One can present equations 2.6 and 2.7 in a clearer form by introducing depth-averaged velocities, U and V, in the x and y directions:

$$\frac{\partial U}{\partial t} + U \frac{\partial U}{\partial x} + V \frac{\partial U}{\partial y} = $$
$$-g \frac{\partial z_h}{\partial x} - \frac{\tau_{bx}}{\rho H} + \frac{\tau_{hx}}{\rho H} + \frac{1}{H} \frac{\partial}{\partial x} \left(H v_t \frac{\partial U}{\partial x} \right) + \frac{1}{H} \frac{\partial}{\partial y} \left(H v_t \frac{\partial U}{\partial y} \right) \tag{2.11}$$

$$\frac{\partial V}{\partial t} + U \frac{\partial V}{\partial x} + V \frac{\partial V}{\partial y} = $$
$$-g \frac{\partial z_h}{\partial y} - \frac{\tau_{by}}{\rho H} + \frac{\tau_{hy}}{\rho H} + \frac{1}{H} \frac{\partial}{\partial x} \left(H v_t \frac{\partial V}{\partial x} \right) + \frac{1}{H} \frac{\partial}{\partial y} \left(H v_t \frac{\partial V}{\partial y} \right) \tag{2.12}$$

The bed shear stress, τ_b, is determined by the Manning-Strickler relation shown by equation 2.13. This equation utilizes the well-known relation between shear stress and dynamic pressure. The product of velocity with magnitude of velocity provides direction for the shear stress. The relation is also a component equation that allows for x and y components of the shear stress.

$$\tau_b = \rho \frac{n^2 g}{R^{1/3}} V|V| \tag{2.13}$$

2.6 General Characterization of Ice Roughness

For singular objects obstructing a flow, a drag model is typically used to represent flow impedance. In this case, the following equation is applicable.

$$F_D = C_D A \frac{\rho V^2}{2} \tag{2.14}$$

In which F_D is the drag force, C_D is a drag coefficient, A is frontal area, r is density, and V is free stream velocity. Power dissipation can be determined using the product of the force and the velocity, or $F_D V$. This provides one way to represent a roughness effect. It has been extended in the past to large formations of repetitive roughness elements, such as vegetation stems. In such cases, the drag coefficient becomes more complex because correlation between the drag coefficients of roughness elements is in close proximity. This correlation is often related to not only the density of roughness elements, but also their arrangements.

2.7 Manning Roughness

Ice surface roughness is an important parameter for predicting the fluid flow along the boundaries of the fluvial system. For open water flow the roughness is related to the discharge and the hydraulic radius of the flow cross section by the Manning's equation. However,

roughness is significantly impacted by the formation fluvial ice formation in northern rivers. The

presence of ice cover in the fluvial system increases hydraulic resistance with the rough ice-

water boundary compared to a relatively smooth air-water boundary (Ehrman et al., 2021).

2.7.1 Roughness Calibration

Chow (1959) casts the general relation between n and k as:

$$n = \phi \left(\frac{R_h}{k} \right) k^{1/6} \tag{2.15}$$

Where n is the Manning roughness, R_h is hydraulic radius, and k is a roughness length

scale. Chow suggested that ϕ is only a weak function of R_h/k, and based on Strickler's (1923)

findings, ϕ can be replaced with a constant:

$$n \approx c_n k^{1/6} \tag{2.16}$$

This relation is confirmed by others, including Strickler (1923), Dingman (2009), and

Sturm (2010), who use different values for c_n depending on the units used for k and the length

scale used to represent k (e.g., D_{50}). The length scale most appropriate for representing k is not

clear-cut, and there has been a lot of research on this topic for rough surfaces. According to

Nikora et al. (1998) there are two groups of thought about representing roughness: using a

characteristic particle size and based on a random field. Nikora et al. (1998) cited a large number

of publications based on the characteristic particle size approach which have found that k is on

the order of about 3 to $3.5D_{84}$, or about $6.8D_{50}$. Disadvantages of such an approach are that

particle shape is not considered, nor is the surface shape of non-particulate roughness elements, a

consideration that could be important for ice structures. The random field approach appears to be

more versatile.

Ehrman et al. (2021) investigated estimation of ice roughness using remotely piloted aircraft and photogrammetry. They recognized that collecting detailed data about ice covers is expensive and dangerous. Ehrman et al. compared roughness measured using SfM photogrammetry with roughness predicted using the Nezhikhovskiy equation in which ice thickness and roughness are interrelated and found good results. It was necessary to hypothesize that the roughness above and below the ice was similar. Their objectives included: testing remote sensing methodologies of measuring surface roughness (on top of the ice cover), identifying metrics of ice roughness measurements, and testing the hypothesis that surface ice roughness and sub-surface ice roughness are related and similar. Regarding the hypothesis, Ehrman et al. referred to Ashton (1986) to point out that surface roughness may not be the same as sub-surface roughness if a jam has been in place for a long enough period of time because of water shear.

Ehrman et al. discussed characterization of roughness by referring to the work of Gomez (1993), Nikora et al. (1998), and Aberle and Nikora (2006) as providing some possible ways to characterize roughness, including the difference between peaks and a locally derived average (Gomez), frequency distributions (Nikora et al.), and statistical components (Aberle and Nikora). To convert from a local roughness height (D) to a spatial roughness (n), research often use a relation of a Strickler form:

$$n \approx c_n D^{1/6} \tag{2.17}$$

Where D is often expressed in sand grain diameters. Ehrman et al. also referred to Manning's roughness values for the underside of ice based on ice thickness, hydraulic radius, and/or roughness height. These equations are those of Nezhikhovskiy (1964):

$$n \approx 0.0252ln(t_i) + 0.0706 \tag{2.18}$$

and Beltaos (2013):

$$n \approx 0.095D^{1/2}R^{1/3} \tag{2.19}$$

While Ehrman et al. suggested that in some cases flow is pressurized, it is unlikely that ice jams are pressurized for most cases in Nebraska, where ice sheets are relatively thin compared to river width and ground anchoring (grounded ice jams) is a common problem.

The detailed procedure to extract roughness described by Ehrman et al. was as follows. In the first step, DEMs were constructed from all point cloud data collected. The DEMs are referred to as high-resolution, but the exact spatial resolution is not clarified. Based on the counts provided in figures, it seems that the resolution is extremely high—probably at least as small as 5 cm by 5 cm.

In the second step, a representative 50 m by 50 m sample (they refer to it as 50 m², but the team interprets they mean 2500 m² based on figures) of the ice was selected that was free from biases associated with banks or other non-ice cover features. In the next (third step), a linear plane was fit to the sample and subtracted from the data to provide a roughness representation instead of an elevation representation. In the fourth step, a 2D Fast Fourier Transform was applied to the sample to remove surface trends not addressed by the planer fit. A band-pass filter was applied to the data with a range of 0.08 to about 70 m.

In the next (fifth) step, the data were further reduced into two sets: one with the full filtered data and a second that just included peaks (using a peak-pick algorithm designed for R).

In the sixth and final step, different potential representations of roughness were determined, including interquartile range and standard deviation of the full data sets and min, max, mean, and 84th percentile of the peak data sets. They found that the best correlations between roughness metrics and Manning's n estimated with Nezhikhovskiy-predicted roughness were when the Standard Deviations or interquartile ranges were used to represent roughness.

2.8 Manning Roughness Calibration

The most important input parameters for two-dimensional ice jam flow are the Manning roughness coefficients for the riverbed, n_b and for the underside ice cover, n_i. The calibration of the Manning roughness coefficient will be the most important step in the two-dimensional ice jam flow model. Rokaya and Lindenschmidt (2020) performed correlation studies on various parameters for modeling river ice with RIVICE, HEC-RAS and RIVJAM. It was found that the roughness of the riverbed n_b and the roughness of the ice sheet n_i are negatively correlated in HEC-RAS. Calibration of n_b is performed for the HEC-RAS ice model by simultaneously adjusting the roughness of ice, n_i and the friction angle φ of the ice jam.

Ice surface roughness is an important parameter for predicting the fluid flow along the boundaries of the fluvial system. For open water flow the roughness is related to the discharge and the hydraulic radius of the flow cross section by the Manning's equation. However, roughness is significantly impacted by the formation fluvial ice formation in northern rivers. The presence of ice cover in the fluvial system increases hydraulic resistance with the rough ice-water boundary compared to the relatively smooth air-water boundary (Ehrman et al., 2021).

One of the empirical equations is given by Nezhikhoskiy (1964) to estimate the roughness of ice, n_i:

$$n_i \approx 0.0252 \ln(t_i) + 0.0706 \tag{2.20}$$

In this equation the constant $c_n = 0.095$ represents the newly formed ice jams. The hydraulic radius R is also included in this equation to include the significant impact of roughness on the hydraulic radius of ice jams. After the ice jam has formed the ice roughness is slowly smoothed from the shear forces developed between water and ice beneath the ice cover (Ehrman et al., 2021).

Beltaos (2001) obtained the Manning's value n_0 for composite layers of the ice cover and riverbed, using a two-layer hypothesis for flow under an ice cover. For an ice jam up to 3 m thick, the composite Manning roughness coefficient, n_0, is in the range of 0.063 to 0.076 $t^{1/2}h^{-1/3}$, where t is the thickness of the ice jam and h is the average depth of the flow under the ice jam.

$$n_0 = 0.0690 t_j^{0.5} h^{-1/3} \; for \; t_j < 3\,m \tag{2.21}$$

Fan et al. (2019) give the relationship for the Manning's roughness coefficient n_i to the thickness of the ice jam for break up jam given below.

$$\begin{aligned} n_i &= 0.0690 H^{-0.23} t_j^{0.40} \; for \; t_j > 1.5\,ft \\ n_i &= 0.0593 H^{-0.23} t_j^{0.77} \; for \; t_j < 1.5\,ft \end{aligned} \tag{2.22}$$

Beltaos (2013) developed another relationship based on the formation of new ice jams (Ehrman et al., 2021).

$$n_i \approx 0.095 D^{\frac{1}{2}} R^{\frac{1}{3}} \tag{2.23}$$

They found that the best correlations between roughness metrics and Manning's n estimated with Nezhikhovskiy-predicted roughness were when the Standard Deviations or interquartile ranges were used to represent roughness.

2.8.1 Manning Roughness Computation for Spencer Dam Site

For one example, the Spencer Dam Failure Investigation Report says ice slabs up to six feet thick have been observed by the locals during the ice run periods (see fig. 2.1). This assumes a conservative value of five feet for ice thickness and water depth of two feet as the maximum flood values used in the 2D-Hydrodynamic ice flow model and uses equation (1) to calculate the composite Manning roughness coefficient and Equation (2) to calculate the ice surface Manning roughness coefficient respectively. The value for n_0 and n_i are 0.056 and 0.074 respectively.

Figure 2.1 2-ft thick ice block (Photo Source: Nebraska Public Power District, March 2019)

Belekon-Sabaneev gives the composite roughness of an ice-covered river channel as:

$$n_c = \left(\frac{n_b^{3/2} + n_i^{3/2}}{2} \right)^{2/3}$$

(2.24)

where n_b and n_i are the Manning roughness coefficients for the bed and ice, respectively.

2.9 Resistance of Ice Crust

Wazney et al. (2015) modified the Michel (1978) equation for resistance between the solid crust and the unconsolidated ice accumulation given below (see Table 2.1).

$$R = \tau_0 h_c + \frac{1}{2} \sin(\phi) \frac{\gamma_w (\gamma_w - \gamma_i)(1 - \rho_j) h^2}{\gamma_i}$$

(2.25)

Table 2.1 Parameters for Resistance During Freeze Up

Parameter	Definition	Magnitude	Unit
R	Resistance force per unit width	Variable	$\frac{kN}{m}$
h_c	Solid Ice Crust Thickness	Variable	m
h	Depth of Water	Variable	m
τ_0	Tangential Strength of Solid Crust	1000	kPa
ϕ	Internal Friction Angle	46^0	deg
γ_w	Specific Weight of Water	9.81	$\frac{kPa}{m}$
γ_i	Specific Weight of Ice	9.02	$\frac{kPa}{m}$
ρ_j	Jam Porosity	0.4	unitless

After substituting the values of the parameters, the following equation is obtained.

$$R = 1000 h_c + 0.185 h^2$$

(2.26)

The first term on the right side of this equation governs the resistance during the freeze up. This has been verified by several experiments on freeze-up processes on river ice Wazney et al. (2015).

2.10 Effects of Sediment Transport and Bed Change

Sediment transportation in channel flow contributes to changes on the bed and thalweg of the river. Ice formation during the freeze-up starts with border ice formed adjacent to the banks due to low velocities in the river. With more freeze-ups over time, all the river is covered with ice related to hydraulic and meteorological conditions (Nyantekyi-Kwakye et al., 2021).

The relationship for Manning's roughness was determined by (Knack & Shen, 2018) by combining early experimental studies and is given below.

$$\frac{n_i}{n_b} = 1.04(\eta \frac{D_{50}}{k_{ice}})^{-0.15} \tag{2.27}$$

In the above equation n_i is the Manning's roughness coefficient of ice cover, n_b is the roughness coefficient of the riverbed, D_{50} is the average size of the sediment, and k_{ice} is the equivalent roughness height of the underside of the ice cover.

η is the ratio of relative flow intensity defined by Knack and Shen (2018) as

$$\eta = \frac{\theta}{\theta_c} \tag{2.28}$$

where θ is the dimensionless flow intensity and θ_c is the critical dimensionless flow intensity, found by

$$\theta = \frac{\tau_{bed}/[(\rho_s/\rho - 1)\rho g D_i]}{\theta_c} \tag{2.29}$$

The ice jam formation affects the sediment transport and bed in an alluvial river. A laboratory experiment on a simulated 1000 m channel, with a width of 10 m, bed slope of 0.001, and discharge of 14.9 m^3/s showed that the ice jam has a thickness 9% greater with bed changes than without bed changes (Knack and Shen, 2018). The Niobrara River and the Loup River both show considerable bed changes as observed from studying the lidar DEM from 2019 before the ice jams occurred and comparing the riverbed morphology to the current condition witnessed by the team's site visits and UAS imagery. Therefore, the thickness of the ice jam can be assumed to be 10% thicker.

2.11 Effects of Temperature

After the ice cover reaches a thickness of one meter, its growth essentially stops because the increased thickness significantly slows heat loss. This reduction in heat loss is further exacerbated by the presence of a thick layer of ice combined with snow cover above it. According to Robert and Tran (2012), these conditions prevent the ice from thickening further.

2.12 Chapter Summary

The chapter provides a comprehensive overview of the formation, characteristics, and impacts of ice jams in rivers, particularly in cold regions. It begins by discussing the economic and infrastructural threats posed by ice jams, especially during spring when melting and breaking ice can cause significant flooding. The chapter delves into the complex flow dynamics beneath ice covers, the processes of frazil and anchor ice formation, and the challenges associated with data collection under ice-covered rivers. It highlights the significant differences between open water flow and ice-covered flow, emphasizing the complexity of predicting ice jam floods due to the higher flow depths associated with ice jams.

The chapter also explores the use of modern technologies, such as uncrewed aerial systems (UAS), for surveying ice-covered rivers, offering a safer and more efficient alternative to traditional methods. It discusses various computer models used to simulate ice jam dynamics, including CRISSP, RIVICE, and HEC-RAS, and their respective capabilities and limitations in modeling ice jams in one or two dimensions. The text further addresses the challenges of calibrating Manning's roughness coefficients for ice-covered rivers, the effects of sediment transport on ice jam formation, and the role of temperature in limiting the growth of ice cover once it reaches a certain thickness. Throughout the chapter, references to studies and empirical equations provide a detailed understanding of the physical processes and modeling techniques related to ice jams.

Chapter 3 Study Sites

3.1 Study Site Selection

In this project, five Nebraska sites were considered: (1) the Missouri River near Omaha, (2) the Loup River near Columbus, (3) the North Loup River in St. Paul, (4) the Niobrara River at the Highway 11 crossing, and (5) the Niobrara River at the Highway 281 crossing. These sites were selected based on their historical ice jam occurrences or if an ice jam developed during the project. The river sites were also based on their differences in flow rates, widths, and other geometric and flow conditions.

3.2 Site 1: Missouri River at Omaha (Omaha)

For the Missouri River site, the survey covered an area of about 2.01 square kilometers. A total of 1,821 images were collected at a flying altitude of 123 meters, capturing the site in high detail. The resulting ground resolution of 1.61 cm/pixel ensures a precise depiction of the river and surrounding areas. Such resolution is critical for detailed hydrological studies and environmental monitoring (see figs. 3.1 and 3.2).

Figure 3.1 UAS-derived orthomosaic image for the Omaha site.
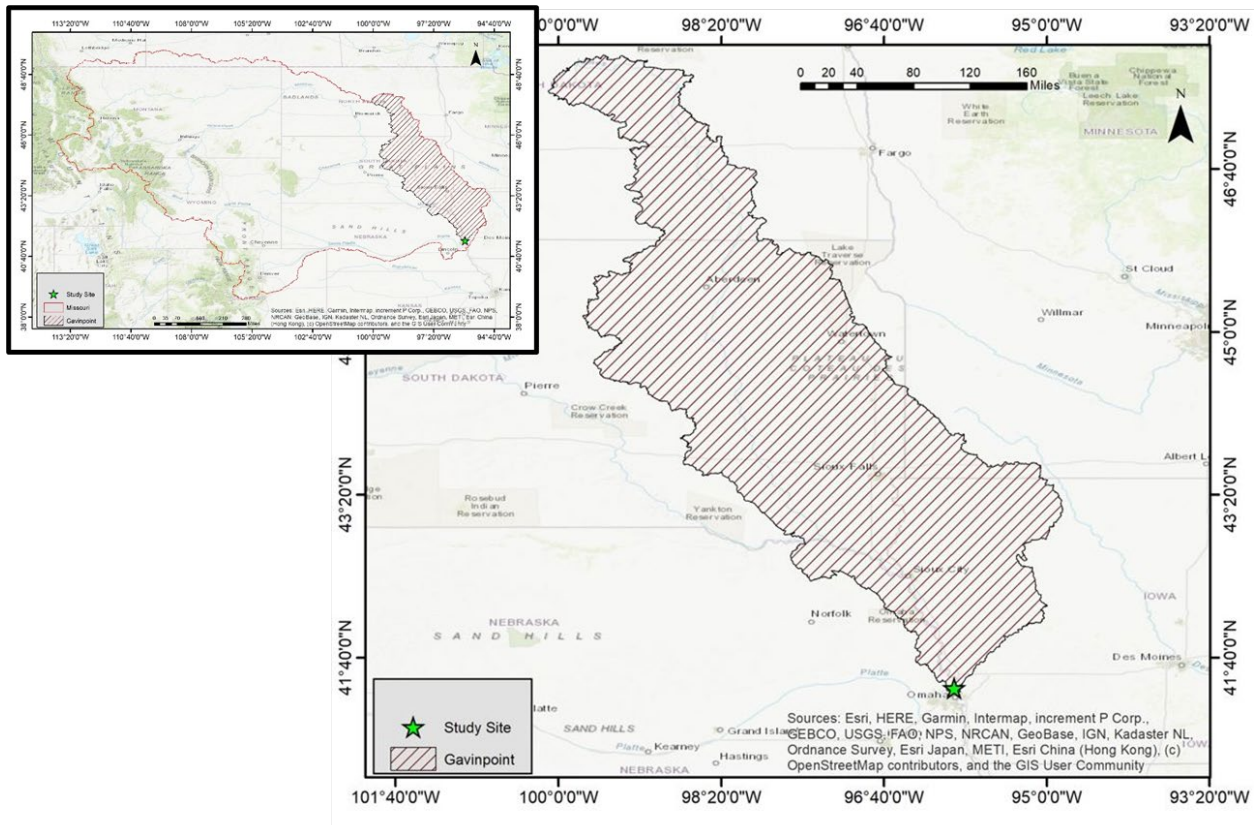
Figure 3.2 Watershed map for the Omaha site.

3.3 Site 2: Loup River near Columbus (Columbus)

The Loop River-Columbus site survey encompassed a large area of 6.65 square
kilometers. This survey captured 7,415 images at a flying altitude of 129 meters, which provided
a thorough overview of the extensive area. This area is larger given its role for modeling as
detailed in later chapters. The data resolution achieved is 1.69 cm/pixel, ensuring that even small
features are clearly represented. This high level of detail is particularly valuable for
comprehensive land and water resource management (see figs. 3.3 and 3.4). In the figure below
(fig. 3.3), this dataset did not include ice and despite past ice jams at this location, one was not
observed during the project period.

Figure 3.3 UAS-derived orthomosaic image for the Columbus site.
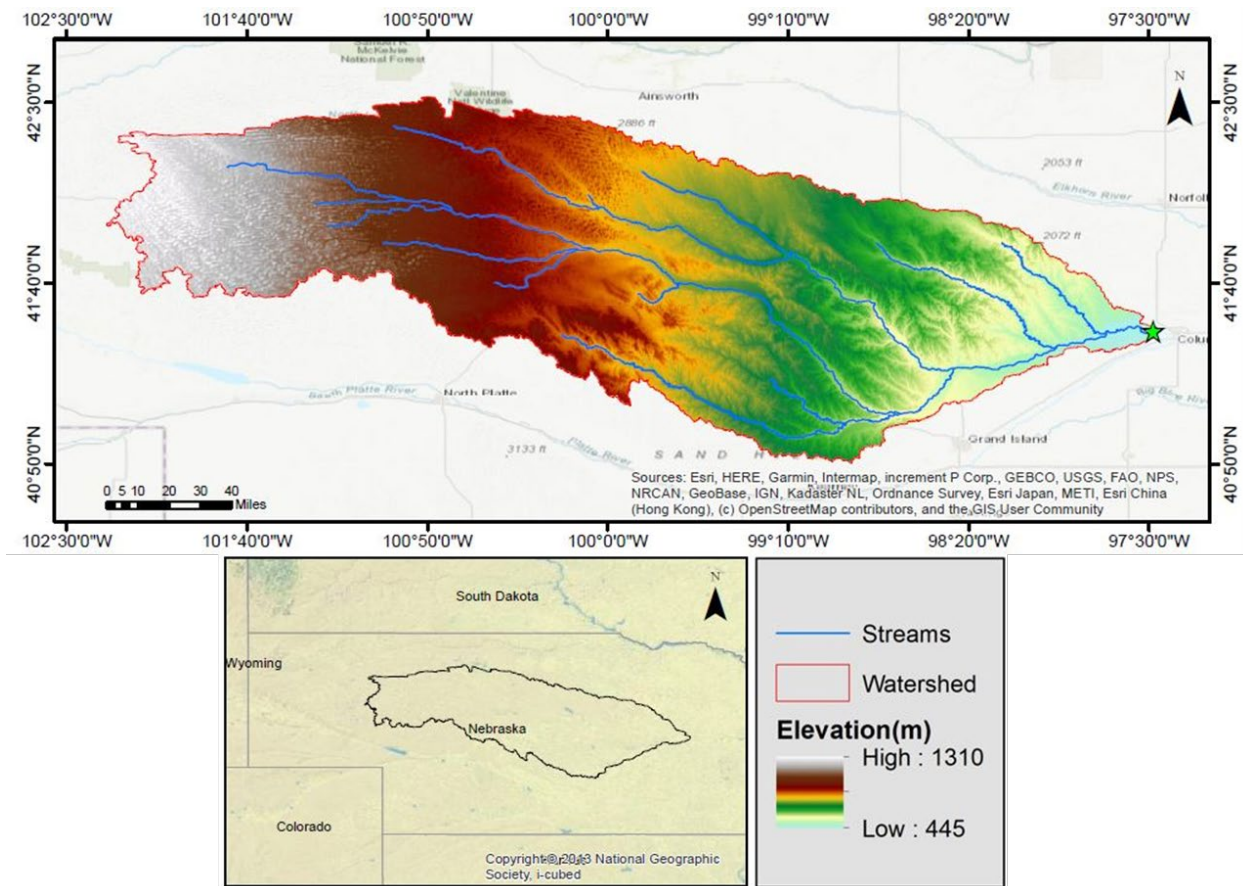
Figure 3.4 Watershed map for the Omaha site.

3.4 Site 3: North Loup River at St. Paul (St. Paul)

The survey of the North Loop-St. Paul site covered an area of approximately 1.07 square kilometers. The survey involved 1,045 images captured from an altitude of 111 meters, providing extensive coverage of the terrain. The processed imagery has a ground resolution of 1.45 cm/pixel, which enables high-definition mapping of the area. This detailed imagery is essential for accurate topographical and infrastructural analysis with the bridge structure (see figs. 3.5 and 3.6).
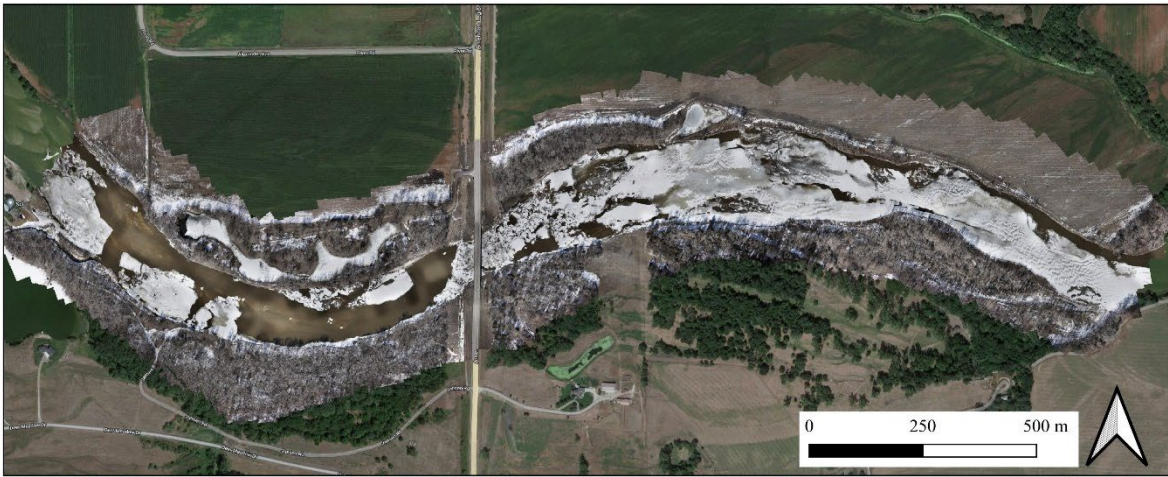
Figure 3.5 UAS-derived orthomosaic image for the St. Paul site.
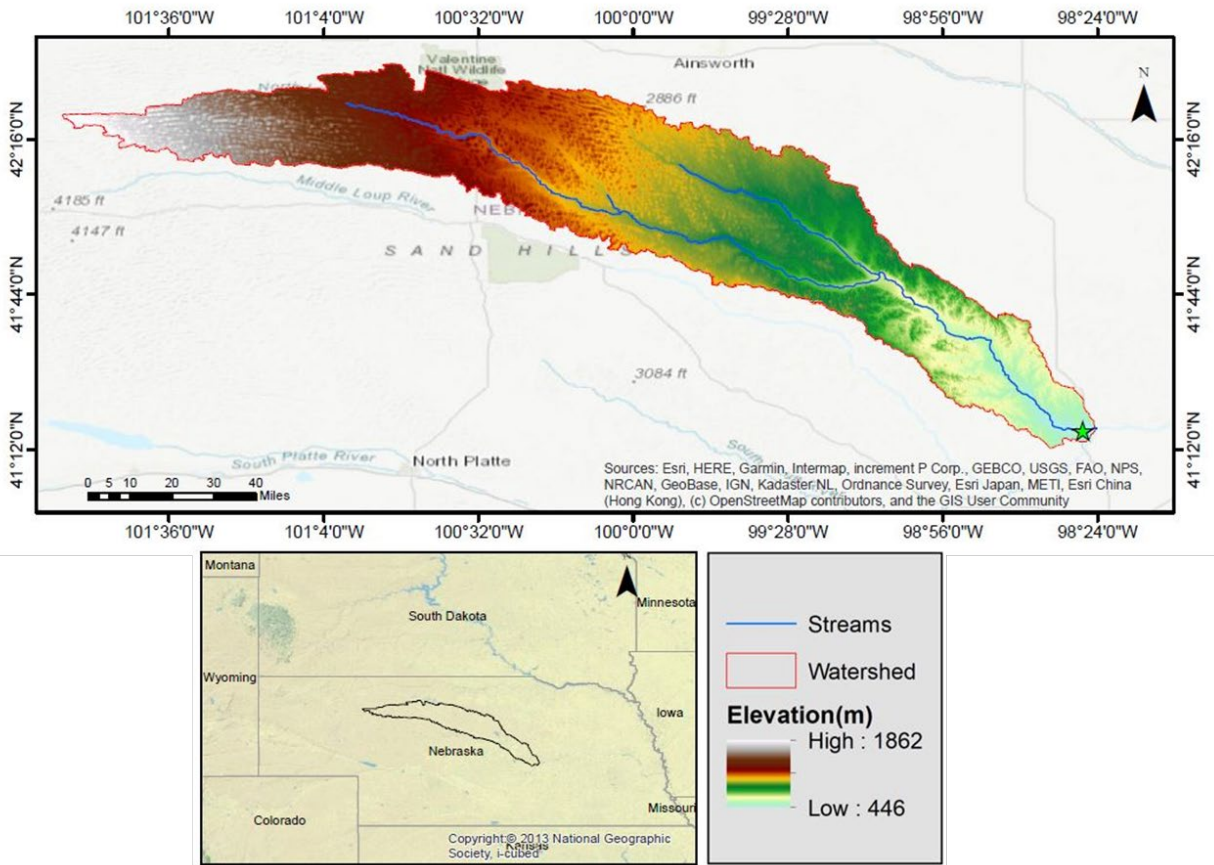
Figure 3.6 Watershed map for the St. Paul site.

The Niobrara-Butte site survey spanned an area of about 3.37 square kilometers. The survey captured 3,749 images at a flying altitude of 128 meters, ensuring comprehensive coverage of the site. The processed data has a ground resolution of 1.66 cm/pixel, allowing for precise surface representation. Such detailed resolution supports in-depth environmental and structural assessments (see figs. 3.7 and 3.8).

Figure 3.7 UAS-derived orthomosaic image for the Butte/Highway 11 site.
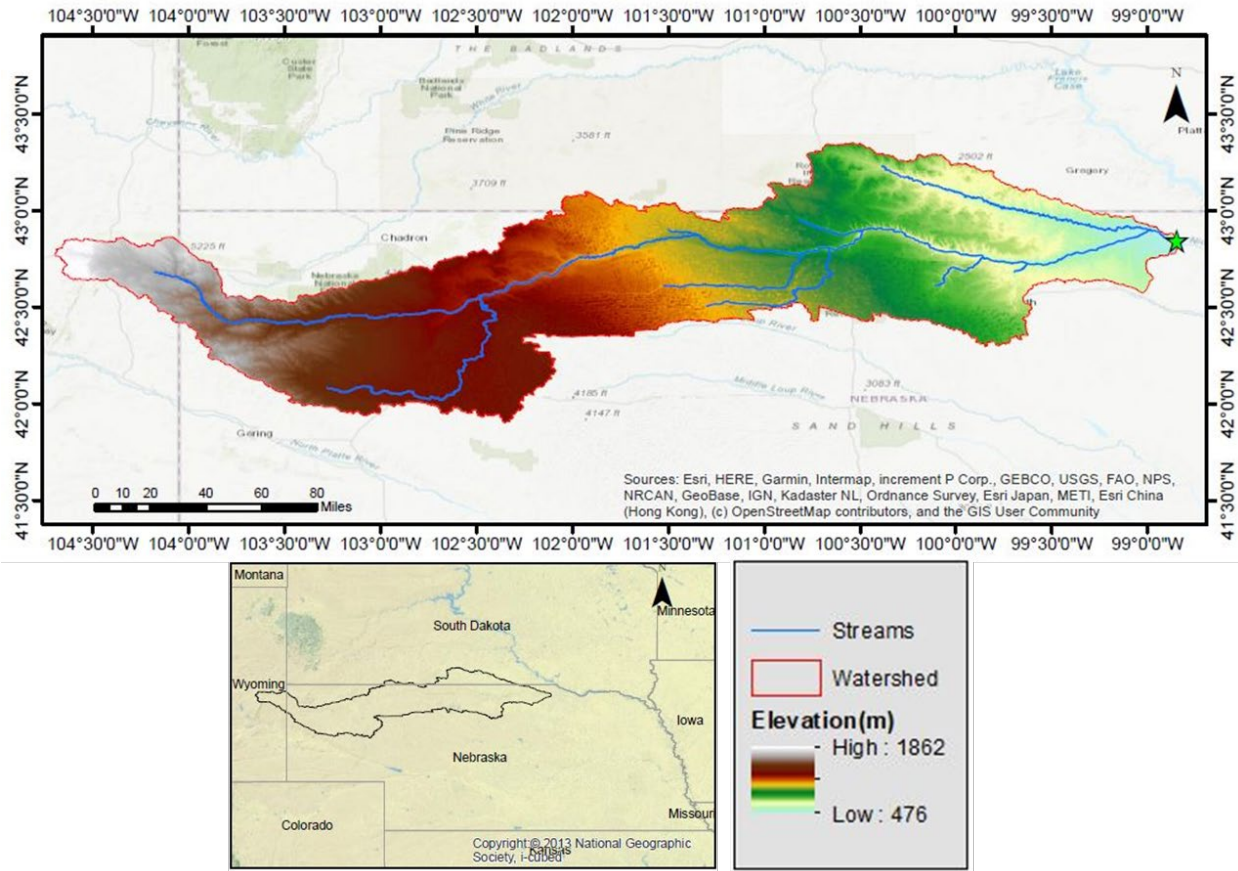
Figure 3.8 Watershed map for the Butte/Highway 11 site.

3.6 Site 5: Niobrara River at Highway 281 (Spencer/Highway 281)

The Niobrara-Spencer site survey covered an area of approximately 3.49 square kilometers. A total of 3,831 images were captured during the survey, which was conducted at a flying altitude of 117 meters. The resulting data has a ground resolution of 1.57 cm/pixel, providing detailed imagery of the site. This high-resolution data is crucial for accurate analysis and mapping of the surveyed area (see figs. 3.9 and 3.10).
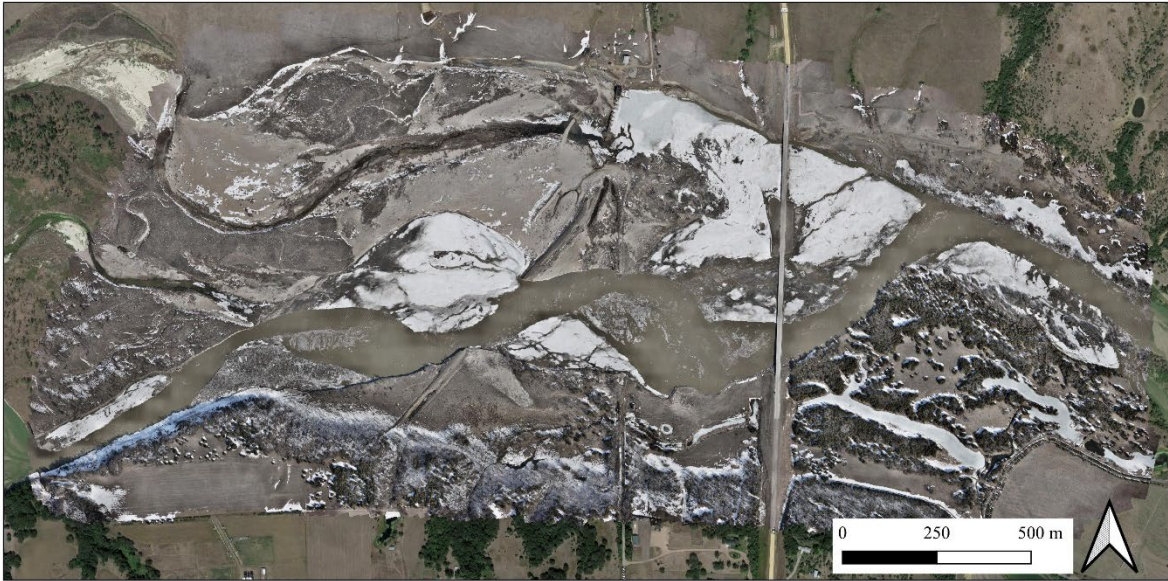
Figure 3.9 UAS-derived orthomosaic image for the Spencer/Highway 281 site.
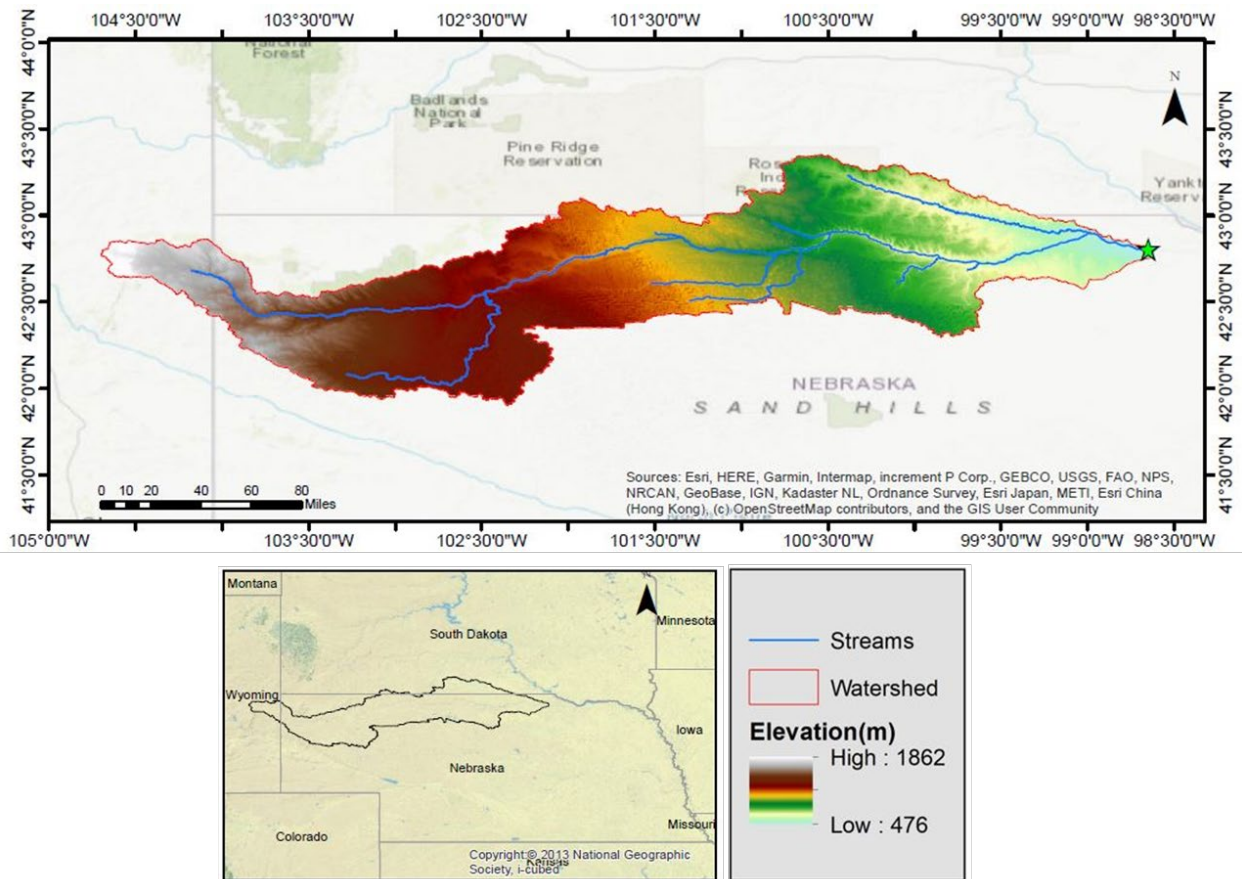
Figure 3.10 Watershed map for the Spencer/Highway 281 site.

3.7 UAS Data Processing

The UAS data consisted of both a set of raw 2D images acquired by the UAS and data from a base station. The base station enabled precise localization of each image, achieving centimeter-level accuracy using the post-processed kinematic technique within surveying. Once the images were geotagged with centimeter-level accuracy, they were processed using structure-from-motion (SfM) software to produce both 2D and 3D data products. The 2D data product is known as an orthomosaic, which aids in identifying and measuring objects in the dataset. The 3D data product is a point cloud, which is a digital representation of the site in terms of the surfaces of objects recorded, as SfM does not penetrate surfaces or tree canopies.

The 3D data used in this study was further processed to extract the ground points. This was done using CloudCompare to filter out noise, classify the ground points, and then rasterize them into a two-meter grid for elevation. This rasterized point cloud was later converted to a .tiff format for use in hydraulic modeling.

3.8 Chapter Summary

In this project, five Nebraska sites were surveyed using uncrewed aerial systems (UASs) to capture high-resolution imagery for detailed environmental and structural analysis. The sites included the Missouri River near Omaha, the Loup River near Columbus, the North Loup River in St. Paul, and two crossings of the Niobrara River. Each site was selected based on historical significance, the occurrence of ice jams, and varying flow and geometric conditions. Thousands of images were captured at each location, resulting in highly detailed orthomosaics and 3D point clouds, which were crucial for hydrological studies and environmental monitoring.

The UAS data was processed using Structure-from-Motion (SfM) software to produce precise 2D and 3D data products. Ground points from the 3D data were further processed,

filtered, and rasterized into a two-meter grid for elevation modeling. This comprehensive data

was then converted into a .tiff format for use in hydraulic modeling, enabling accurate analysis

and mapping of the surveyed areas

Chapter 4 UAS Ice Jam Characteristics

4.1 Overview to Project

Accurate measurement and analysis of ice thickness are crucial for understanding the hydraulic impacts of ice cover on river flow conditions. Building on the work detailed in the previous chapter, which involved the selection and UAS-based surveying of the sites in Nebraska, this study implements a structured methodology to quantify ice thickness and derive Manning's n, a key parameter in modeling flow resistance due to ice. The primary objectives of this study are to measure ice thickness across different river segments using advanced data processing techniques and to calculate Manning's n through comprehensive statistical analysis. These goals are essential for improving the accuracy of hydraulic models, which are used to predict flow behavior and manage ice-related challenges in river systems.

4.2 Methodology

The methodology employed in this study for measuring and analyzing ice thickness involves a systematic sequence of data processing and statistical analysis steps as shown in Figure 4.1. Initially, the regions of interest are segmented to isolate areas where ice thickness measurements will be performed. A Statistical Outlier Removal (SOR) filter, with parameters n equals six and σ equals one, is applied to eliminate noise and outliers, ensuring the accuracy of subsequent ice profile segmentation. The segmented ice profiles are then analyzed in terms of flow-parallel and flow-perpendicular profiles, which are crucial for understanding variations in ice thickness relative to the direction of river flow. Following this, the three-dimensional ice thickness data is projected into a two-dimensional representation, simplifying the analysis of ice features. A linear regression model is applied to the two-dimensional data to explore relationships between ice thickness and other variables, with residuals calculated to assess the

model's accuracy. Several statistical measures, including the median ice thickness, standard deviation (SD), interquartile range (IQR), and mode, are computed to provide a comprehensive understanding of the ice thickness distribution. Finally, Manning's n is calculated using two approaches: one based on the logarithm of ice thickness (Nezhikhoskiy, 1964) and another using a formula related to the interquartile range (Ehrman et al., 2021). These calculations are critical for hydraulic modeling and understanding the flow resistance introduced by the ice. This structured methodology ensures accurate ice thickness measurements and robust statistical analysis, supporting reliable hydraulic modeling and environmental assessments.
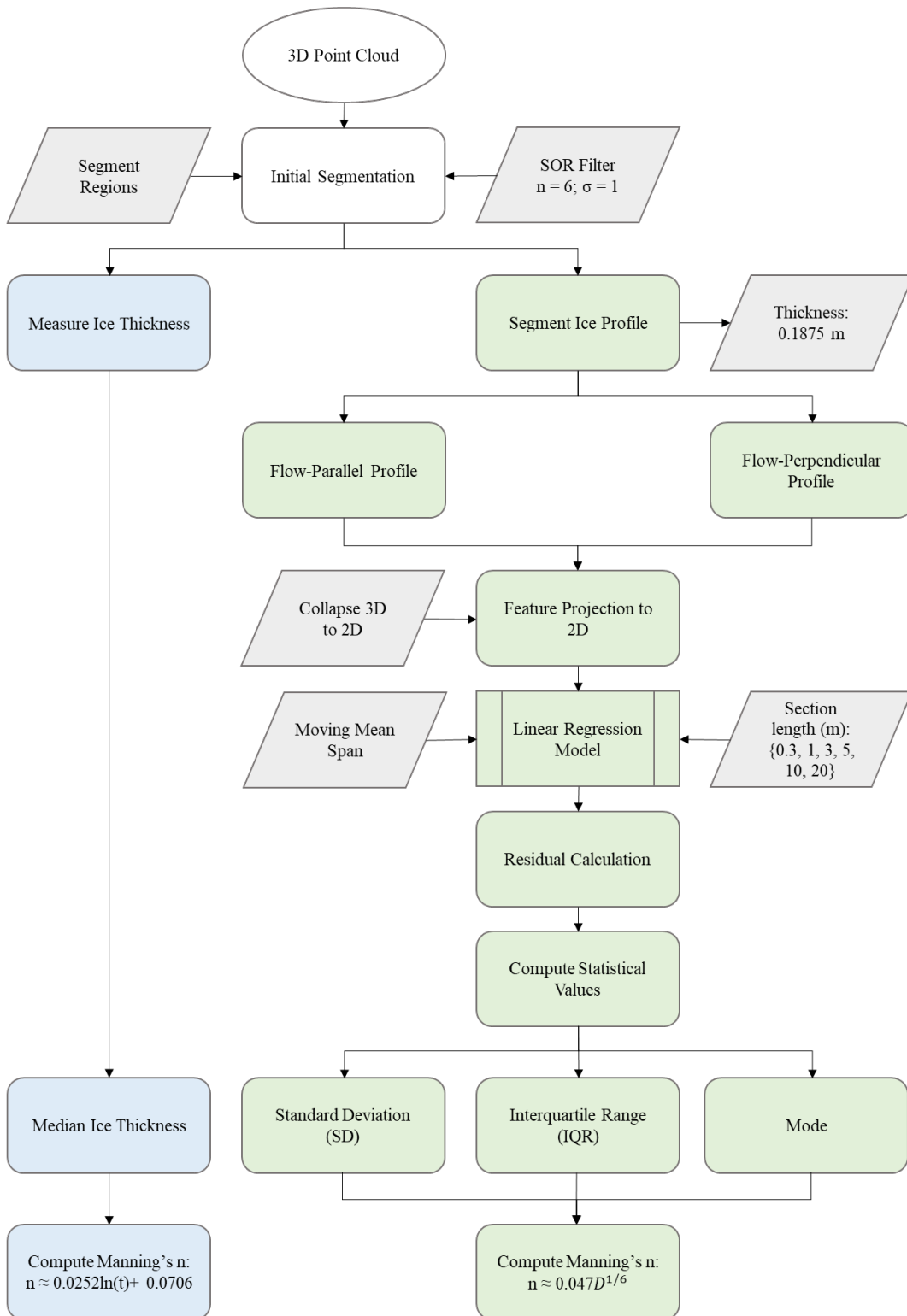
Figure 4.1 Workflow of Manning's n estimation.

4.3 Ice Thickness Determination

Ice thickness values were determined from the 3D point cloud data using segmentation. This was performed at four of the five sites, as no ice data was available at the Columbus site. However, one additional downriver site from St. Paul is included here, known as the Loop River at Fullerton.

The first site selected for measurements was the ice jam on the Niobrara River at Spencer/Highway 281. The ice in this region was notably rough, with numerous rotated and vertically tilted ice pieces observed. Measurements were attempted from the middle section of the ice, ensuring that they were well distributed across all parts of the ice chunk. Figures 4.2 illustrates the distribution of the segmented ice in the Niobrara River ice jam.

To achieve the thickness of the ice in Cloud Compare, several steps were followed. The point cloud was initially imported into Cloud Compare separately. Noise and erroneous points were manually removed from the cloud. A Statistical Outlier Removal (SOR) filter was then applied, using six points and a standard deviation of one. The river section of the cloud was separated from the initial cloud, and the view was adjusted to focus on the vertical and rotated ice chunks. After detecting an ice section, the view was changed to a top-down perspective, and a cross-sectional view of the ice was segmented. The small ice section was then adjusted to provide a better view of its profile. It is important to note that, at this stage, the small, segmented region was visualized, with periodic opening and closing of the whole region's view to ensure the correct part of the ice segment was being analyzed. Finally, the measuring tool was used to determine the distance between the two sides of the ice piece. Table 4.1 presents the thickness measurements for the Niobrara River Spencer site. At this site, 20 measurements were taken, and statistical parameters were also computed to guide the hydraulic model.
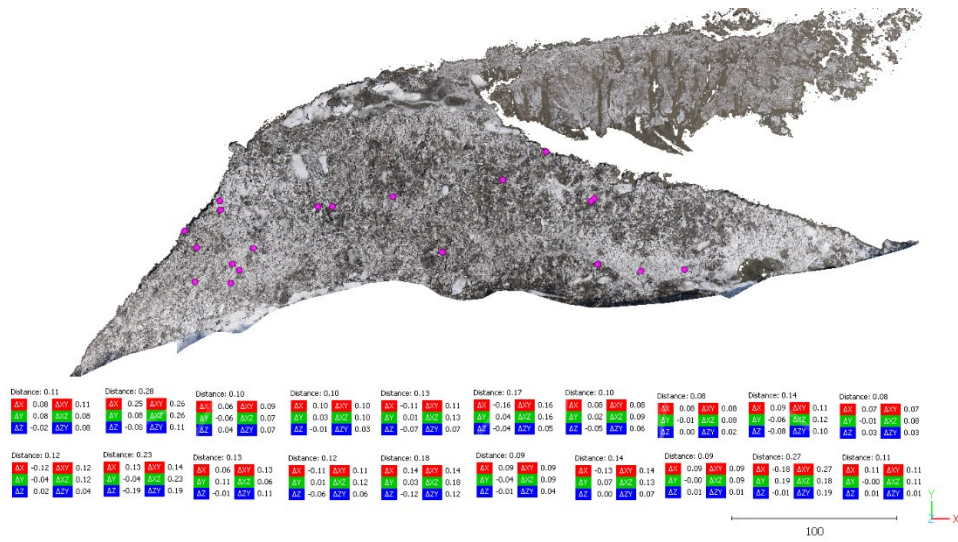
Figure 4.2 Dense point cloud and the location of the measurement.

Table 4.1 Measured ice thickness at Niobrara River at Spencer (Highway 281).

Location ID	Thickness (m)
1	0.11
2	0.28
3	0.1
4	0.1
5	0.13
6	0.23
7	0.21
8	0.08
9	0.14
10	0.23
11	0.12
12	0.23
13	0.13
14	0.12
15	0.18
16	0.09
17	0.14
18	0.09
18	0.16
20	0.11
Mean	0.16
Median	0.13

The second site selected for thickness measurements was the North Loup River in St. Paul. This site featured very smooth ice, which made measurements somewhat challenging. Additionally, a significant number of birds were observed on the ice on the west side of the site. To avoid the removal of small, rough ice pieces, the site was not strictly cleaned; only erroneous points were removed. Consequently, some noise in the data is associated with the presence of the birds. Furthermore, a layer of snow covering the ice made measurement more difficult. Figure 4.3 illustrates the location of the segmented ice section in the North Loup River in St. Paul. As shown in Figure 4.3, most of the rotated and vertical ice was located at the edge of the ice where it met the river, potentially due to water forces or the clearing of the snow cover by river flow. Given the small size of this site, only six measurements were extracted.

As depicted in Figure 4.3, the downstream side of the river was primarily covered with snow, and there was no vertical ice suitable for measurement in that section. Elevation differences were used in some measurements, as the ice pieces had slipped on top of each other, and due to the snow cover, no sharp edges were available for accurate measurements. Table 4.2 also presents the thickness measurements for the North Loup River in St. Paul.
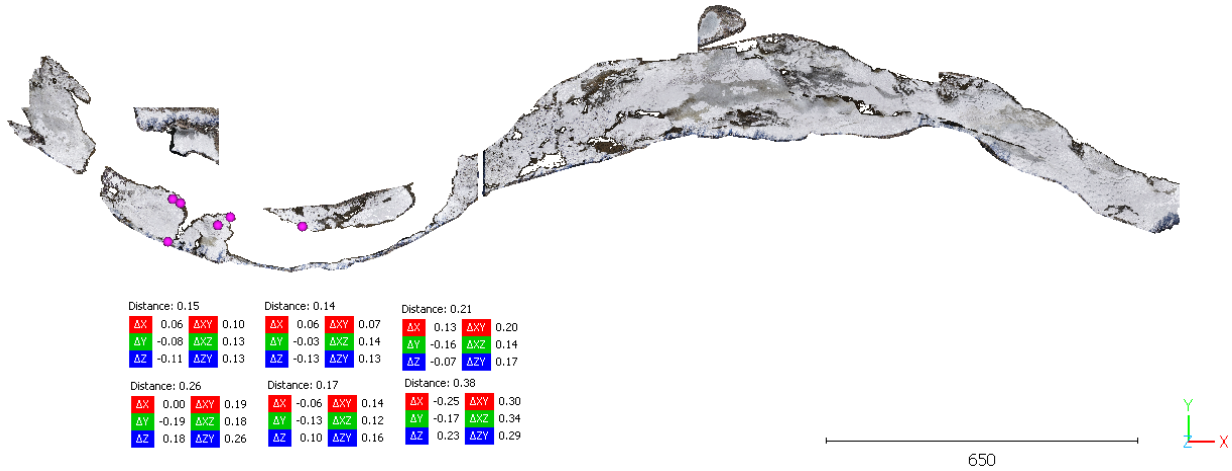
Figure 4.3 Dense point cloud and the location of the measurement For Loop River at St. Paul.

Table 4.2 Measured ice thickness at the Loop River at St. Paul.

Location ID	Thickness (m)
1	0.15
2	0.13
3	0.21
4	0.18
5	0.10
6	0.38
Mean	0.19
Median	0.16

The third set of measurements was conducted on the Loup River at Fullerton. Similar to the other Loup River site, the ice in this location was very smooth. Figures 4.4 and 4.5 show the first and second regions of the ice jam in this river, which were divided into two parts due to the size of the data. Table 4.3 presents the thickness measurements and cross-sectional views of the ice sections for all the measurements in both regions, with a total of ten measurements taken.

The fourth set of measurements was conducted on the Niobrara River at Highway 11. Figures 4.6 – 4.8 display the three regions of the ice jam in this river. Table 4.4 provides the thickness measurements of the ice sections for all the measurements in both regions, with a total

of 16 measurements taken. The fifth and final set of measurements was conducted on the

Missouri River. One notable observation at this site was the presence of several continuous

cracks throughout the ice. Figures 4.9 and 4.10 show the first and second regions of the ice jam

in this river. Table 4.5 presents the thickness measurements of the ice sections for all the

measurements in both regions, with a total of 20 measurements taken.
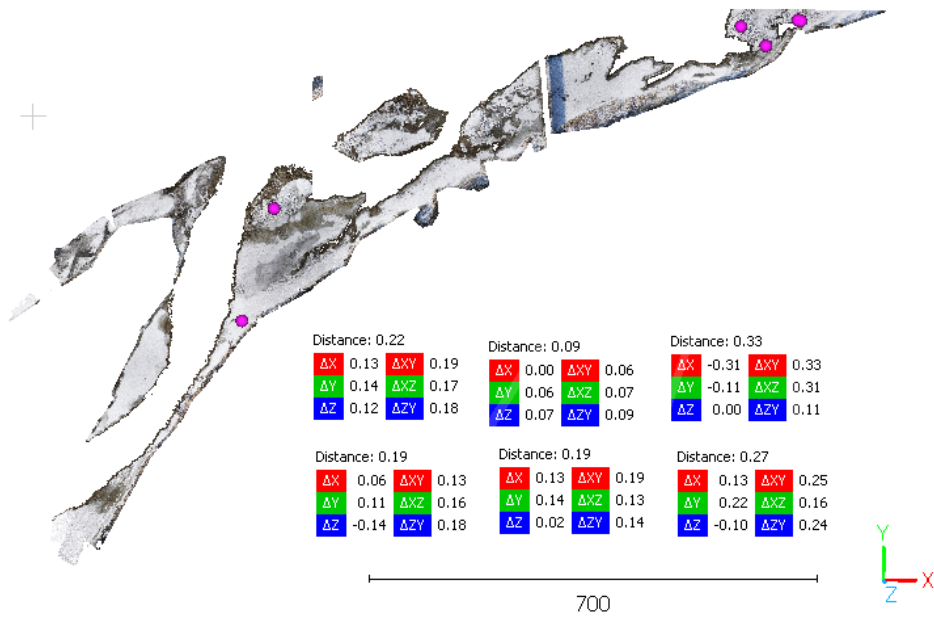
Figure 4.4 Dense point cloud and the location of the measurement For Loop River at Fullerton region one.
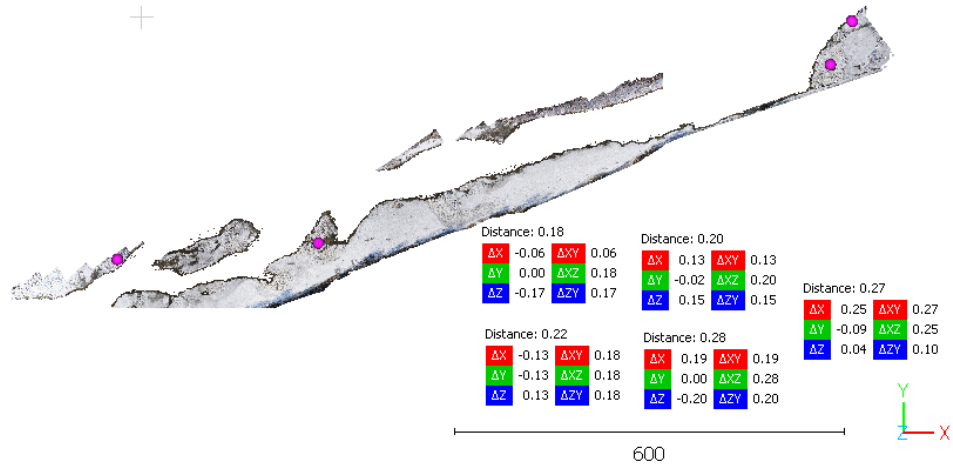
Figure 4.5 Dense point cloud and the location of the measurement at Loop River at Fullerton region 2.

Table 4.3 Measured ice thickness at Loop River at Fullerton.

Location ID	Thickness (m)
1	0.12
2	0.07
3	0.33
4	0.19
5	0.19
6	0.27
7	0.27
8	0.22
9	0.28
10	0.19
Mean	0.24
Median	0.24
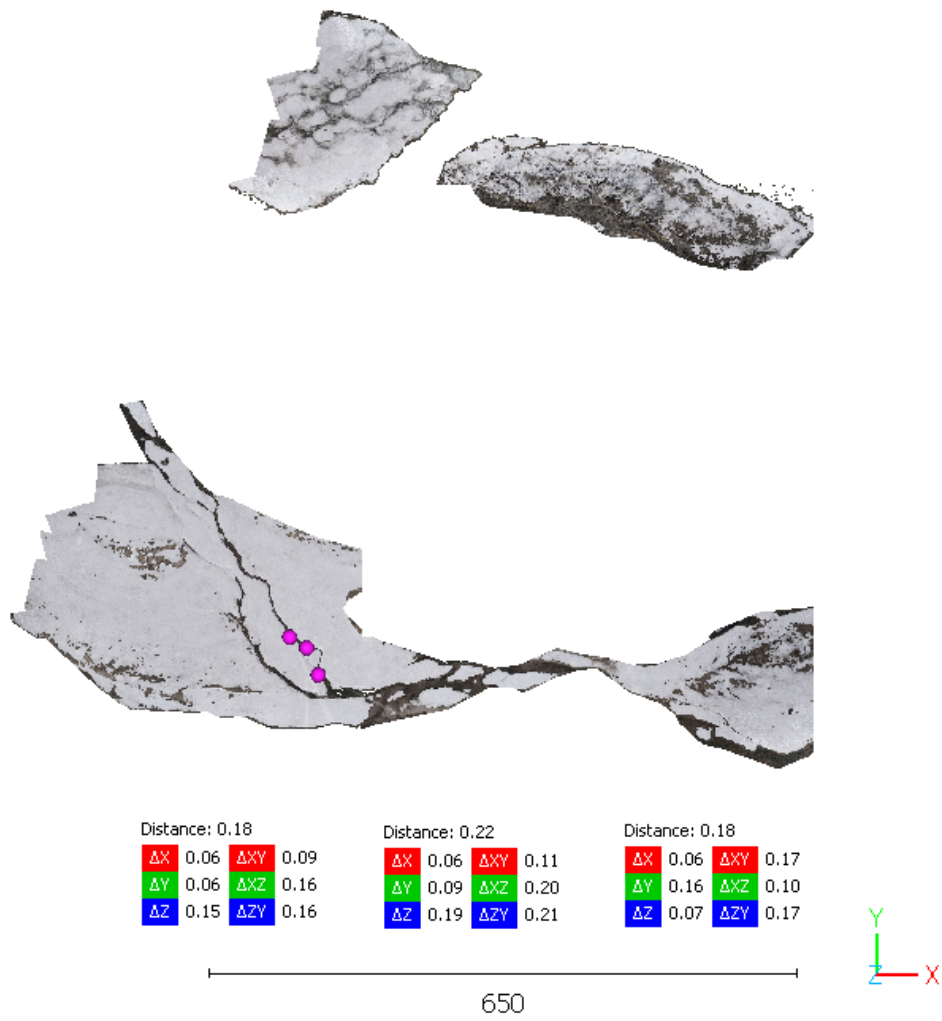
Figure 4.6 Dense point cloud and the location of the measurement at Niobrara River at Butte (Highway 11) (part 1).
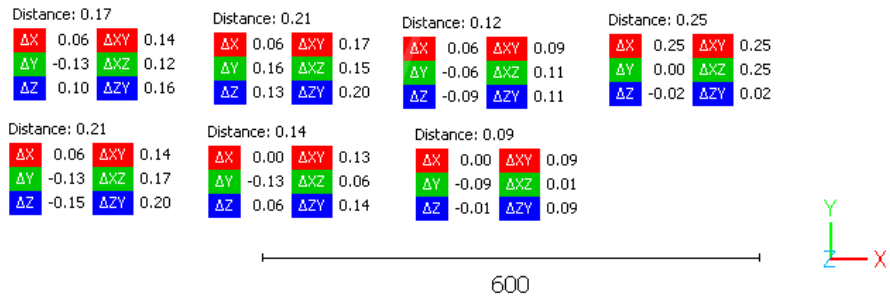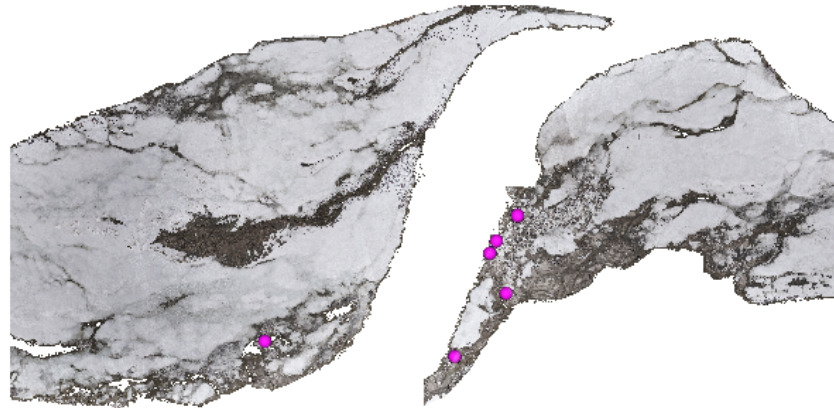
Figure 4.7 Dense point cloud and the location of the measurement at Niobrara River at Butte (Highway 11) (part 2).
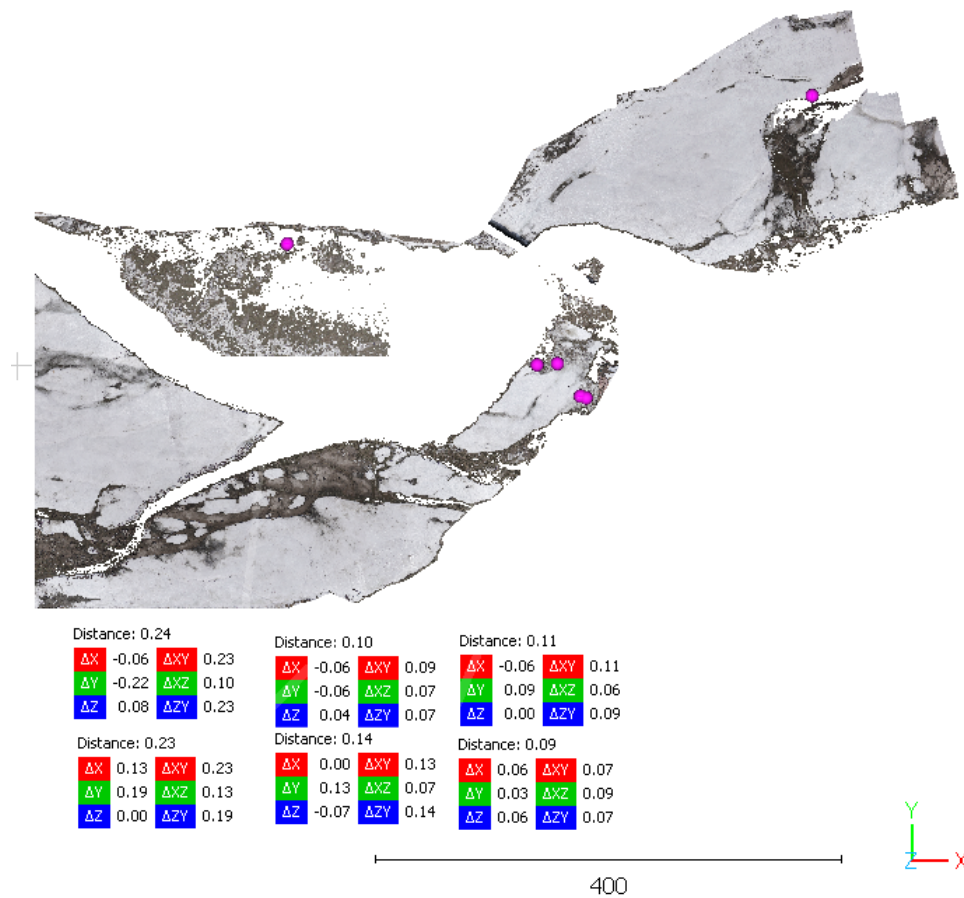
Figure 4.8 Dense point cloud and the location of the measurement at Niobrara River at Butte (Highway 11) (part 3).

Table 4.4 Measured ice thickness at Niobrara River at Butte (Highway 11).

Location ID	Thickness (m)
1	0.18
2	0.22
3	0.18
4	0.11
5	0.10
6	0.23
7	0.09
8	0.14
9	0.09
10	0.12
11	0.21
12	0.25
13	0.21
14	0.17
15	0.14
16	0.25
Mean	0.17
Median	0.18
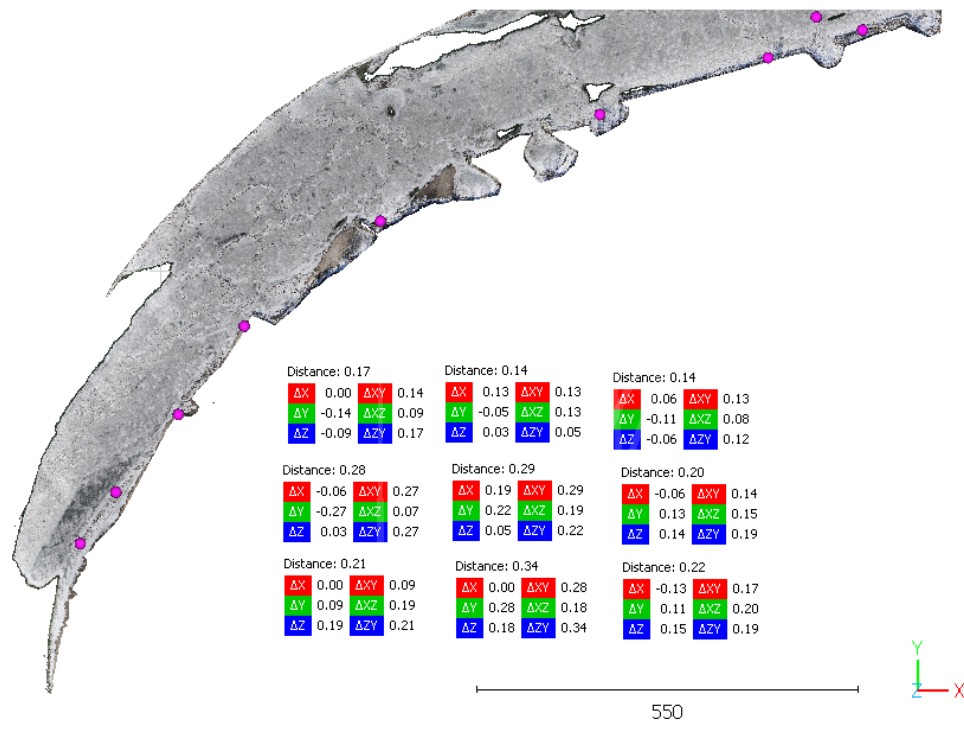
Figure 4.9 Dense point cloud and the location of the measurement at Missouri River at Omaha (part 1).
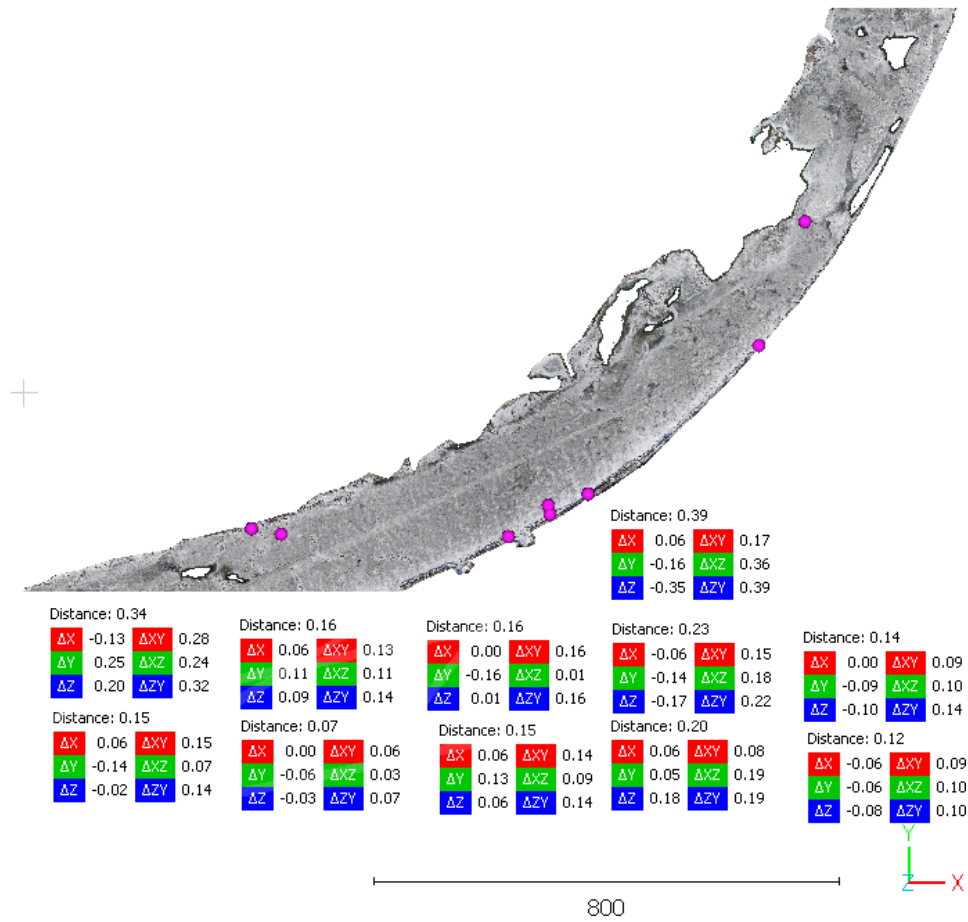
Figure 4.10 Dense point cloud and the location of the measurement at Missouri River at Omaha (part 2).

Table 4.5 Measured ice thickness at Missouri River at Omaha.

Location ID	Thickness (m)
1	0.28
2	0.17
3	0.14
4	0.21
5	14
6	0.29
7	0.22
8	0.34
9	0.20
10	0.16
11	0.20
12	0.15
13	0.16
14	0.12
15	0.07
16	0.39
17	0.15
18	0.23
18	0.14
20	0.34
Mean	0.20
Median	0.18

4.4 Ice Thickness Statistics

The statistical parameters for ice thickness, including the mean, median, and standard deviation, were analyzed and compared across the five measurement sites: Niobrara River at Highway 281, North Loup River in St. Paul, Loup River in Fullerton, Niobrara River at Highway 11, and Missouri River. The results of this comparison are presented in Table 4.6. As illustrated in this table, the standard deviation of ice thickness at all sites is relatively small, indicating a limited range of variation in the measurements. This low standard deviation suggests that the ice thickness at each site is consistent, with measurements closely clustered around the mean.

Moreover, the comparison between the mean and median values reveals that these two parameters are nearly equal at each site. This similarity indicates a symmetric distribution of the ice thickness data. In a symmetric distribution, the mean and median are close in value, implying that the data does not have significant skewness and that most of the measurements fall within a specific, narrow range.

For example, the mean ice thickness at the Loop River in Fullerton is 0.24 meters, with a median of 0.24 meters and a standard deviation of 0.04 meters. The equal mean and median, coupled with the low standard deviation, confirm the consistency and symmetry of the ice thickness distribution at this site. Similarly, the Niobrara River at the Highway 281 site shows a mean of 0.14 meters and a median of 0.12 meters with a standard deviation of 0.06 meters, again indicating a narrow and symmetric distribution of ice thickness.

Across all five sites, these statistical comparisons suggest that the ice thickness measurements are not only consistent but also follow a symmetric distribution, with minimal deviation from the central tendency. This consistency across different sites enhances the reliability of the measurements and provides a clear understanding of the ice conditions in these regions.

Table 4.6 Median thickness and corresponding Manning's n values for all study sites.

Study area	t_{median} (m)	n
Loop River Fullerton	0.24	0.031
Loop River St_Paul	0.16	0.025
Niobrara_HW11	0.18	0.026
Niobrara_HW281	0.13	0.019
Missouri	0.18	0.028

4.5 Ice Roughness Computation

        Uncrewed Aerial System (UAS) data played a crucial role in estimating Manning's

number, a key parameter directly used in the modeling process described in the next chapter.

Due to the absence of ice data at the Columbus site, the focus was placed on the two Niobrara

River sites for this analysis, but all available data was processed as summarized below.

4.5.1 Ice Roughness Computation at Niobrara River Site at Highway 281

        To compute Manning's number, a specific ice chunk in the Niobrara River at the

Highway 281 site was selected to generate the roughness height histogram. Figure 4.11

illustrates the chosen ice chunk for roughness calculations. Five locations within this ice chunk

were selected for ice thickness measurements, following the same methodology as in previous

tasks. The thickness values obtained, as presented in Table 4.1, were subsequently used in

Nazikhovskiy's equation to calculate ice roughness, also presented in Table 4.7.
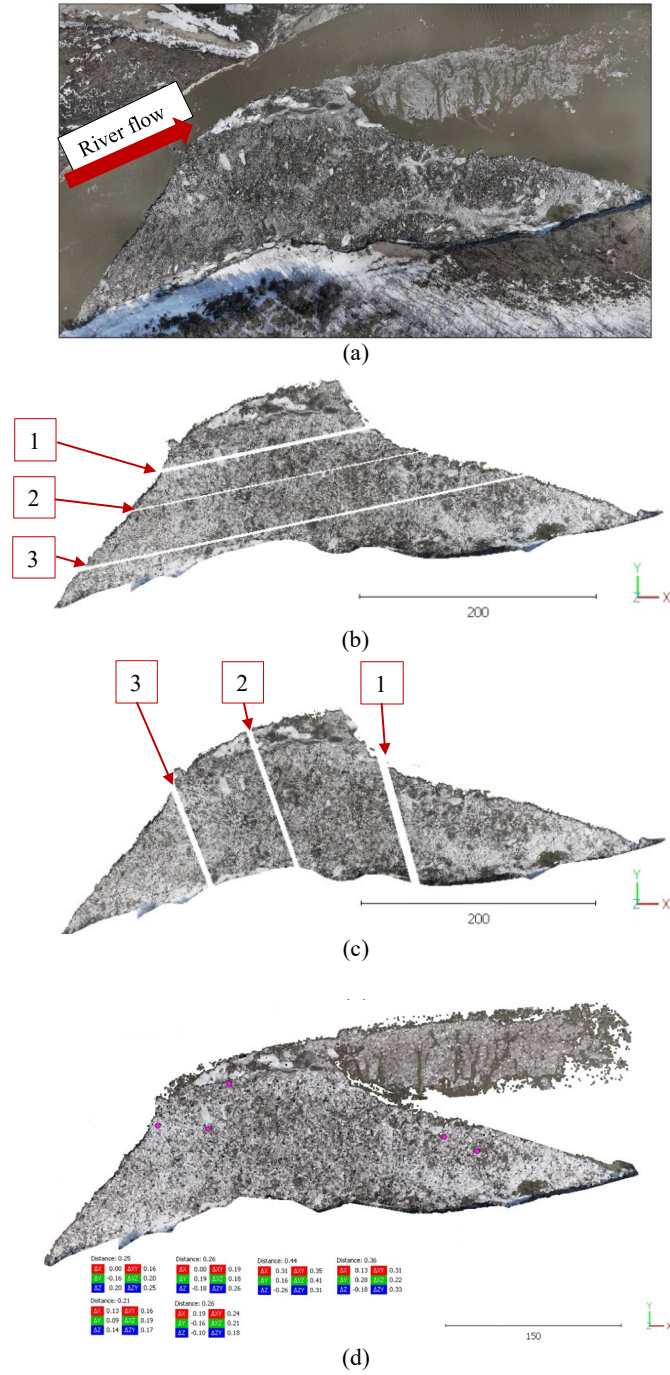
Figure 4.11 Mapping of the ice jam in Niobrara River at Spencer (Highway 281). (a) Position and the river water flow; (b) dense point cloud and the location of the parallel profiles; (c) dense point cloud and the location of the perpendicular profiles; (d) locations of the thickness measurement

Table 4.7 Statistical calculations were performed for each section's length and its corresponding Manning's n using the Nazikhovskiy equation for the Niobrara River at Spencer (Highway 281).

Location ID	Thickness (m)	n (m)
1	0.26	0.037
2	0.25	0.036
3	0.36	0.045
4	0.21	0.036
5	0.26	0.031
Mean	0.27	0.037
Median	--	0.037

While the Nazikhovskiy equation offers a straightforward and simple method for calculating roughness, an alternative approach was implemented to enhance the confidence in these estimates. This alternative method involved analyzing the distribution of roughness using data derived from UAS imagery. Specifically, UAS imagery was utilized to generate a 3D point cloud and a 2D orthomosaic of the study sites, from which the ice surface Manning's n was measured and compared across different profiles.

To compute the UAS-derived ice Manning's n, the process began with the importation of the ice jam point cloud into Cloud Compare. A small strip was then selected, consisting of three parallel profiles and three perpendicular profiles relative to the river flow. The data was subsequently imported into MATLAB for further processing. Noisy points and outliers were removed using a smoothing function, where the data was subdivided into sections of 150 points each, and the mean value of each section replaced the original data points, effectively reducing noise and outliers. The smoothed profile data was then segmented into smaller section lengths, and a line was fitted to the dataset using the mean values (see fig. 4.12). To determine the optimal section length, profiles were processed with various lengths, including 0.3 m, 1 m, 5 m, 10 m, and 20 m, for comparison purposes. A line was fitted to the data points over each section

length, and the difference between each data point and the best-fitted line was calculated and recorded as the residual data for that specific region. Figure 2 illustrates the points in the section length with the best-fitted line for Parallel Profile #3. Using the residual data, a histogram was generated for each profile. For instance, Figure 4.13 presents the residual data distribution for Parallel Profile #1 with a section length of 10 meters, and additional profile data distributions are provided in Table 4.8.
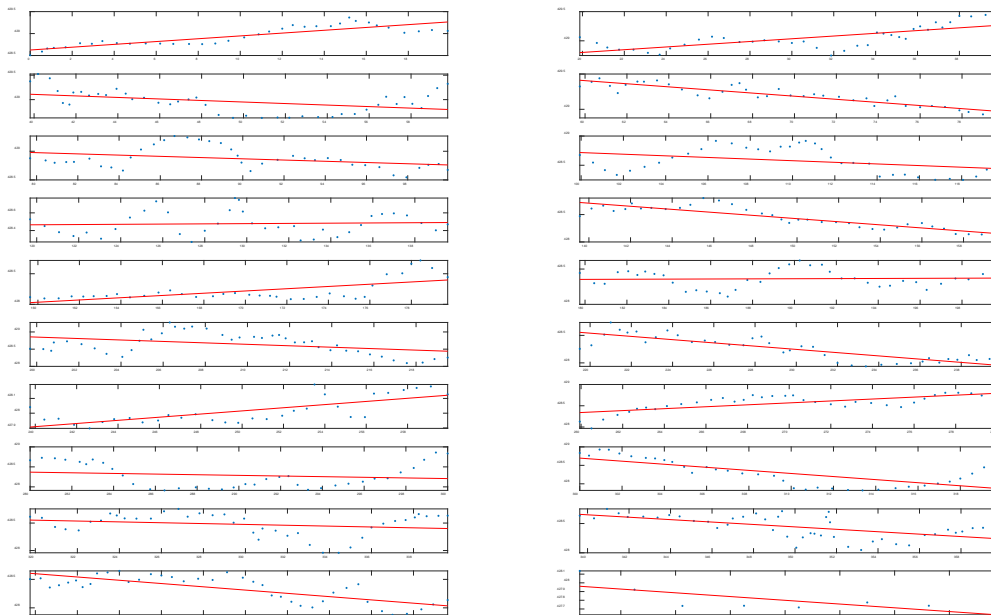
Figure 4.12 Segmented cross-section of profile #3 at Niobrara River with the best-fit line in each section of 20 m Niobrara River at Spencer (Highway 281).
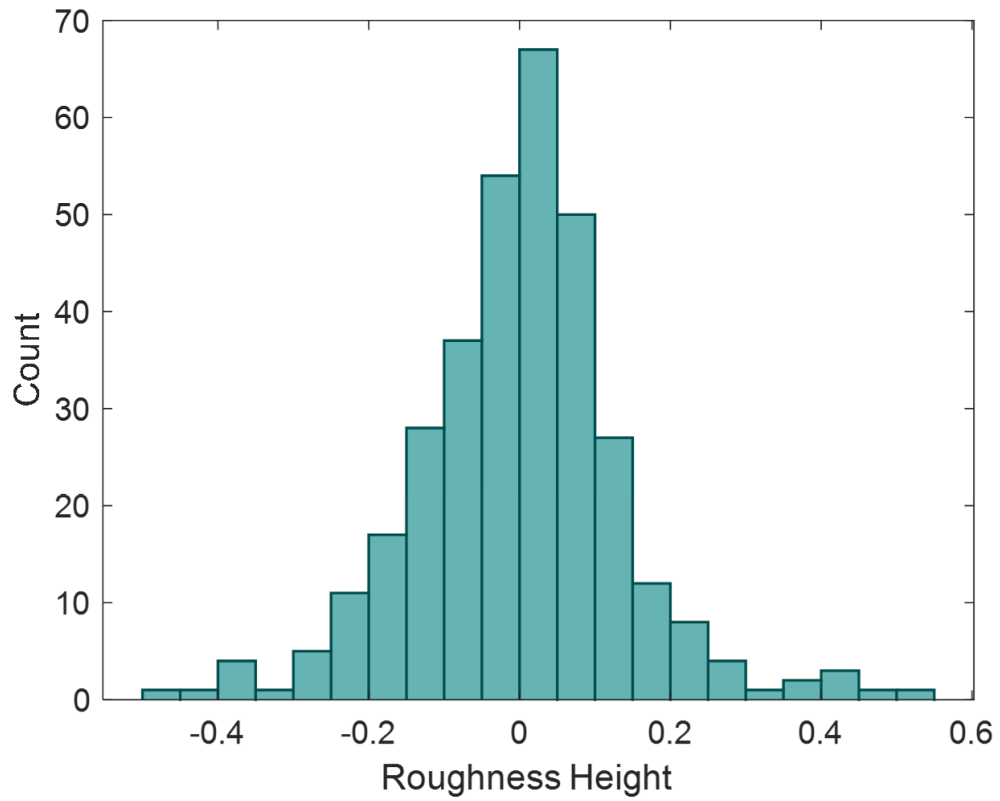
Figure 4.13 Roughness height histogram for the profile parallel to river flow Niobrara River at Spencer (Highway 281).

Table 4.8 Manning's n estimation for various section lengths Niobrara River at Spencer (Highway 281).

Profile region	Direction	Metrics	L= 0.3 m	L = 1 m	L = 3 m	L = 5 m	L = 10 m	L = 20 m
1_1	Para	IQR	0.0000	0.0004	0.0220	0.0237	0.0266	0.0288
		SD	0.0003	0.0207	0.0239	0.0251	0.0273	0.0290
		Mode	0.0000	0.0000	0.0325	0.0334	0.0336	0.0377
1_2	Para	IQR	0.0003	0.0004	0.0200	0.0216	0.0241	0.0259
		SD	0.0003	0.0175	0.0212	0.0230	0.0247	0.0273
		Mode	0.0000	0.0000	0.0298	0.0312	0.0327	0.0340
1_3	Para	IQR	0.0003	0.0240	0.0311	0.0324	0.0349	0.0366
		SD	0.0214	0.0268	0.0309	0.0322	0.0336	0.0352
		Mode	0.0000	0.0000	0.0380	0.0383	0.0393	0.0403
1_4	Para	IQR	0.0003	0.0213	0.0298	0.0309	0.0329	0.0357
		SD	0.0003	0.0264	0.0299	0.0313	0.0327	0.0345
		Mode	0.0000	0.0000	0.0375	0.0405	0.0408	0.0436
1_5	Para	IQR	0.0003	0.0242	0.0298	0.0314	0.0335	0.0361
		SD	0.0179	0.0262	0.0291	0.0308	0.0327	0.0339
		Mode	0.0000	0.0000	0.0359	0.0381	0.0389	0.0408
1_6	Para	IQR	0.0003	0.0004	0.0215	0.0235	0.0273	0.0306
		SD	0.0003	0.0199	0.0232	0.0254	0.0279	0.0294
		Mode	0.0000	0.0000	0.0288	0.0318	0.0349	0.0357
1_7	Para	IQR	0.0000	0.0004	0.0220	0.0234	0.0265	0.0288
		SD	0.0003	0.0203	0.0231	0.0255	0.0271	0.0288
		Mode	0.0000	0.0000	0.0321	0.0354	0.0357	0.0337
1_1	Perp	IQR	0.0000	0.0092	0.0212	0.0228	0.0275	0.0293
		SD	0.0003	0.0214	0.0251	0.0255	0.0276	0.0291
		Mode	0.0000	0.0003	0.0316	0.0327	0.0331	0.0355
1_2	Perp	IQR	0.0003	0.0004	0.0229	0.0264	0.0297	0.0327
		SD	0.0003	0.0201	0.0248	0.0265	0.0309	0.0323
		Mode	0.0000	0.0000	0.0310	0.0319	0.0380	0.0380
1_3	Perp	IQR	0.0003	0.0184	0.0250	0.0274	0.0308	0.0350
		SD	0.0003	0.0231	0.0264	0.0286	0.0300	0.0326
		Mode	0.0000	0.0000	0.0306	0.0345	0.0361	0.0361
1_4	Perp	IQR	0.0003	0.0242	0.0293	0.0324	0.0371	0.0368
		SD	0.0127	0.0269	0.0298	0.0317	0.0346	0.0353
		Mode	0.0000	0.0003	0.0381	0.0404	0.0405	0.0416

Profile region	Direction	Metrics	L= 0.3 m	L = 1 m	L = 3 m	L = 5 m	L = 10 m	L = 20 m
1_5	Perp	IQR	0.0003	0.0262	0.0317	0.0330	0.0348	0.0377
		SD	0.0203	0.0269	0.0303	0.0320	0.0337	0.0360
		Mode	0.0000	0.0003	0.0371	0.0387	0.0394	0.0414
1_6	Perp	IQR	0.0003	0.0246	0.0303	0.0321	0.0348	0.0363
		SD	0.0198	0.0268	0.0307	0.0330	0.0348	0.0360
		Mode	0.0000	0.0000	0.0380	0.0407	0.0439	0.0452
1_7	Perp	IQR	0.0000	0.0138	0.0268	0.0281	0.0302	0.0314
		SD	0.0003	0.0221	0.0264	0.0269	0.0301	0.0319
		Mode	0.0000	0.0000	0.0319	0.0312	0.0349	0.0364
2_1	Para	IQR	0.0000	0.0004	0.0209	0.0233	0.0265	0.0291
		SD	0.0003	0.0189	0.0226	0.0241	0.0266	0.0286
		Mode	0.0000	0.0000	0.0298	0.0301	0.0326	0.0346
2_2	Para	IQR	0.0000	0.0003	0.0213	0.0227	0.0259	0.0288
		SD	0.0003	0.0180	0.0215	0.0230	0.0254	0.0276
		Mode	0.0000	0.0000	0.0270	0.0290	0.0318	0.0351
2_3	Para	IQR	0.0003	0.0099	0.0207	0.0226	0.0260	0.0280
		SD	0.0003	0.0184	0.0215	0.0230	0.0255	0.0273
		Mode	0.0000	0.0000	0.0310	0.0310	0.0319	0.0356
2_4	Para	IQR	0.0000	0.0004	0.0198	0.0217	0.0241	0.0274
		SD	0.0003	0.0163	0.0204	0.0221	0.0248	0.0273
		Mode	0.0000	0.0000	0.0277	0.0299	0.0315	0.0344
2_5	Para	IQR	0.0000	0.0121	0.0202	0.0219	0.0252	0.0291
		SD	0.0003	0.0175	0.0209	0.0235	0.0259	0.0292
		Mode	0.0000	0.0000	0.0287	0.0337	0.0342	0.0379
2_1	Perp	IQR	0.0000	0.0004	0.0212	0.0232	0.0262	0.0294
		SD	0.0003	0.0195	0.0228	0.0253	0.0286	0.0300
		Mode	0.0000	0.0000	0.0323	0.0366	0.0377	0.0377
2_2	Perp	IQR	0.0000	0.0004	0.0209	0.0221	0.0259	0.0284
		SD	0.0003	0.0192	0.0229	0.0262	0.0308	0.0329
		Mode	0.0000	0.0000	0.0304	0.0369	0.0422	0.0421
2_3	Perp	IQR	0.0000	0.0004	0.0211	0.0228	0.0271	0.0296
		SD	0.0003	0.0213	0.0249	0.0280	0.0319	0.0340
		Mode	0.0000	0.0000	0.0337	0.0393	0.0439	0.0437
2_4	Perp	IQR	0.0000	0.0004	0.0229	0.0259	0.0298	0.0333
		SD	0.0003	0.0185	0.0240	0.0263	0.0289	0.0313
		Mode	0.0000	0.0000	0.0296	0.0325	0.0335	0.0355

Profile region	Direction	Metrics	L= 0.3 m	L = 1 m	L = 3 m	L = 5 m	L = 10 m	L = 20 m
2_5	Perp	IQR	0.0003	0.0101	0.0228	0.0250	0.0283	0.0302
		SD	0.0003	0.0187	0.0235	0.0250	0.0279	0.0297
		Mode	0.0000	0.0000	0.0291	0.0312	0.0336	0.0363
3_1	Para	IQR	0.0003	0.0004	0.0213	0.0237	0.0274	0.0291
		SD	0.0003	0.0202	0.0272	0.0278	0.0287	0.0297
		Mode	0.0000	0.0003	0.0374	0.0379	0.0361	0.0322
3_2	Para	IQR	0.0000	0.0004	0.0260	0.0270	0.0290	0.0303
		SD	0.0003	0.0229	0.0269	0.0272	0.0290	0.0299
		Mode	0.0000	0.0000	0.0000	0.0000	0.0000	0.0365
3_3	Para	IQR	0.0000	0.0004	0.0206	0.0222	0.0237	0.0276
		SD	0.0003	0.0175	0.0201	0.0219	0.0238	0.0263
		Mode	0.0000	0.0000	0.0267	0.0279	0.0315	0.0315
3_4	Para	IQR	0.0000	0.0004	0.0198	0.0213	0.0245	0.0264
		SD	0.0003	0.0161	0.0206	0.0222	0.0246	0.0270
		Mode	0.0000	0.0000	0.0284	0.0288	0.0332	0.0327
3_1	Perp	IQR	0.0000	0.0004	0.0241	0.0258	0.0302	0.0341
		SD	0.0003	0.0255	0.0312	0.0334	0.0371	0.0391
		Mode	0.0000	0.0000	0.0419	0.0428	0.0438	0.0436
3_2	Perp	IQR	0.0000	0.0004	0.0205	0.0221	0.0244	0.0268
		SD	0.0143	0.0178	0.0213	0.0227	0.0250	0.0269
		Mode	0.0000	0.0000	0.0288	0.0314	0.0325	0.0354
3_3	Perp	IQR	0.0000	0.0004	0.0212	0.0223	0.0247	0.0266
		SD	0.0196	0.0253	0.0279	0.0300	0.0321	0.0354
		Mode	0.0000	0.0000	0.0396	0.0420	0.0444	0.0440
4_1	Para	IQR	0.0000	0.0004	0.0209	0.0220	0.0227	0.0236
		SD	0.0003	0.0201	0.0226	0.0236	0.0241	0.0247
		Mode	0.0000	0.0000	0.0300	0.0347	0.0343	0.0320
4_2	Para	IQR	0.0000	0.0155	0.0223	0.0240	0.0273	0.0296
		SD	0.0003	0.0188	0.0226	0.0241	0.0272	0.0292
		Mode	0.0000	0.0000	0.0300	0.0320	0.0341	0.0352
4_3	Para	IQR	0.0000	0.0004	0.0199	0.0215	0.0242	0.0271
		SD	0.0003	0.0171	0.0204	0.0222	0.0245	0.0270
		Mode	0.0000	0.0000	0.0287	0.0303	0.0306	0.0327
4_4	Para	IQR	0.0000	0.0146	0.0222	0.0238	0.0269	0.0289
		SD	0.0003	0.0204	0.0240	0.0251	0.0271	0.0284
		Mode	0.0000	0.0000	0.0003	0.0352	0.0350	0.0378

Profile region	Direction	Metrics	L= 0.3 m	L = 1 m	L = 3 m	L = 5 m	L = 10 m	L = 20 m
4_1	Perp	IQR	0.0000	0.0004	0.0213	0.0223	0.0242	0.0295
		SD	0.0003	0.0178	0.0214	0.0235	0.0245	0.0306
		Mode	0.0000	0.0003	0.0257	0.0286	0.0276	0.0343
4_2	Perp	IQR	0.0003	0.0003	0.0225	0.0229	0.0245	0.0318
		SD	0.0003	0.0196	0.0246	0.0268	0.0310	0.0341
		Mode	0.0000	0.0003	0.0320	0.0347	0.0369	0.0398
4_3	Perp	IQR	0.0000	0.0139	0.0215	0.0229	0.0247	0.0274
		SD	0.0003	0.0192	0.0232	0.0251	0.0274	0.0286
		Mode	0.0000	0.0000	0.0310	0.0371	0.0397	0.0400
4_4	Perp	IQR	0.0000	0.0004	0.0203	0.0218	0.0240	0.0274
		SD	0.0003	0.0187	0.0212	0.0225	0.0241	0.0267
		Mode	0.0000	0.0000	0.0289	0.0296	0.0299	0.0329
4_5	Perp	IQR	0.0000	0.0003	0.0216	0.0228	0.0261	0.0281
		SD	0.0003	0.0189	0.0222	0.0236	0.0260	0.0269
		Mode	0.0000	0.0000	0.0003	0.0003	0.0003	0.0323

Finally, statistical parameters were calculated for all six profiles within the ice chunk. Table 4.8 presents the statistics for each profile at different section lengths, including mean, median, mode, standard deviation (SD), and interquartile range (IQR). The analysis of the Niobrara site at Highway 281 revealed that the data distribution and range remained relatively consistent for section lengths greater than one meter. However, for section lengths longer than 10 meters, the standard deviation and mode increased significantly, while the mean and median remained nearly zero. This finding suggests a centralized distribution where the best-fitted plane effectively divides the data into positive and negative residual sections.

Given these observations, a section length of 10 meters was identified as the most suitable for Manning's n calculation. This choice is supported by the fact that the mode, which

indicates the most frequently occurring value was zero, and the standard deviation was approximately twice the interquartile range, representing an almost normally distributed dataset.

A preliminary comparison of Manning's n, calculated using the Nazikhovskiy formula and the statistical parameters derived from the six selected profiles, shows that the standard deviation and the formula-calculated Manning's n are closely aligned. This consistency across different methods provides confidence in the reliability of the estimated Manning's n values.

4.5.2 Ice Roughness Computation at Niobrara River Site at Highway 281

A similar methodology was applied at the Niobrara River site at Highway 11. Given the smoother appearance of the ice in this region compared to the Niobrara River at Highway 281, the selection of an appropriate section length was crucial (see fig. 4.14). While a section length of more than one meter was deemed necessary due to the smoother ice surface, for consistency amongst all of the analysis, a section length of 10 meters was selected for the calculation of Manning's n.

The results from this approach are summarized in Table 4.9, which presents the calculated statistics for the UAS-measured data residuals. The mode, representing the most frequently occurring value, was found to be close to zero, and the standard deviation was approximately twice the interquartile range (IQR), indicating an almost normally distributed dataset.

In the preliminary results, a comparison of Manning's n calculated using the Nazikhovskiy formula with the statistical parameters derived from the four selected profiles shows a close alignment between the standard deviation and the formula-calculated Manning's n at the 10-meter section length. This consistency further supports the reliability of the Manning's n estimates for this site, validating the use of the 10-meter section length for these calculations.

For completeness, all Manning's n values as determined from the roughness for various section lengths are presented below (see Tables 4.10 – 4.12). The recommended Manning's n value as determined from the sites are shown in Table 4.6 based solely on the thickness.

(a)

(b)
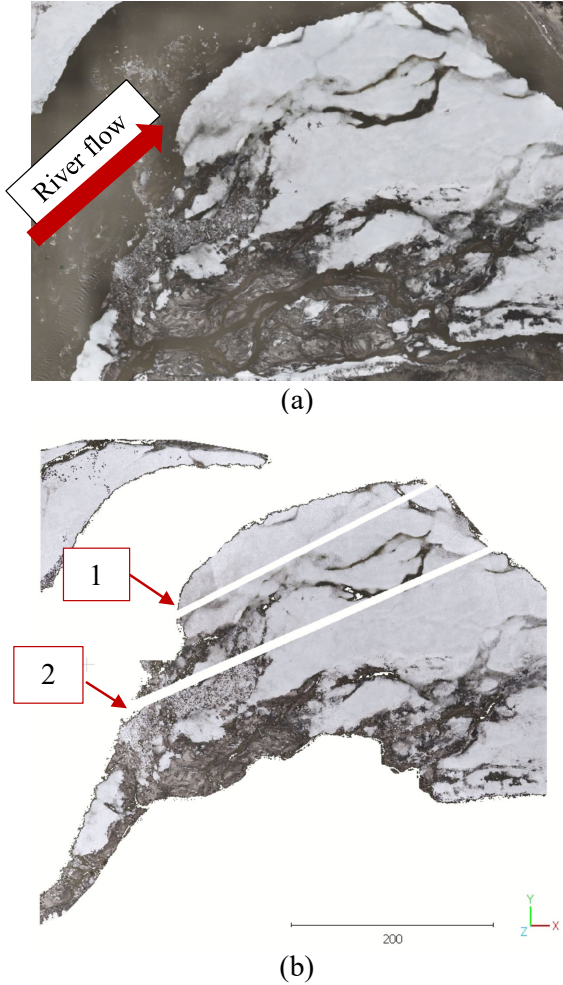
Figure 4.14 Mapping of the ice jam at Niobrara River at Butte (Highway 11). (a) Position and the river water flow; (b) dense point cloud and the location of the parallel profiles; (c) dense point cloud and the location of the perpendicular profiles; (d) locations of the thickness measurement.

(c)

Distance: 0.25

ΔX	0.25	ΔXY	0.25
ΔY	0.00	ΔXZ	0.25
ΔZ	-0.02	ΔZY	0.02

Distance: 0.21

ΔX	0.06	ΔXY	0.17
ΔY	0.16	ΔXZ	0.15
ΔZ	0.13	ΔZY	0.20

Distance: 0.21

ΔX	0.06	ΔXY	0.14
ΔY	-0.13	ΔXZ	0.17
ΔZ	-0.15	ΔZY	0.20

Distance: 0.14

ΔX	0.00	ΔXY	0.13
ΔY	-0.13	ΔXZ	0.06
ΔZ	0.06	ΔZY	0.14

Distance: 0.17

ΔX	0.06	ΔXY	0.14
ΔY	-0.13	ΔXZ	0.12
ΔZ	0.10	ΔZY	0.16

Distance: 0.12

ΔX	0.06	ΔXY	0.09
ΔY	-0.06	ΔXZ	0.11
ΔZ	-0.09	ΔZY	0.11

350
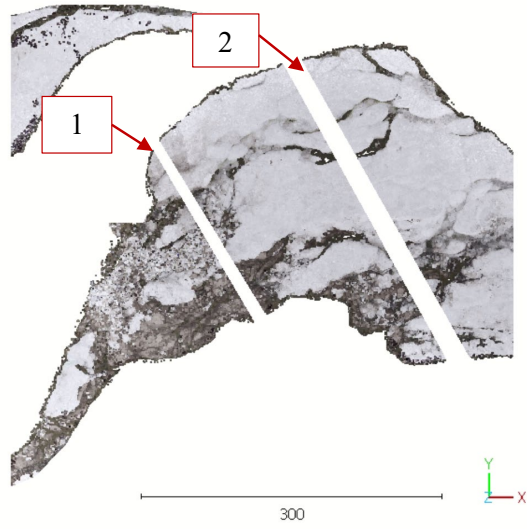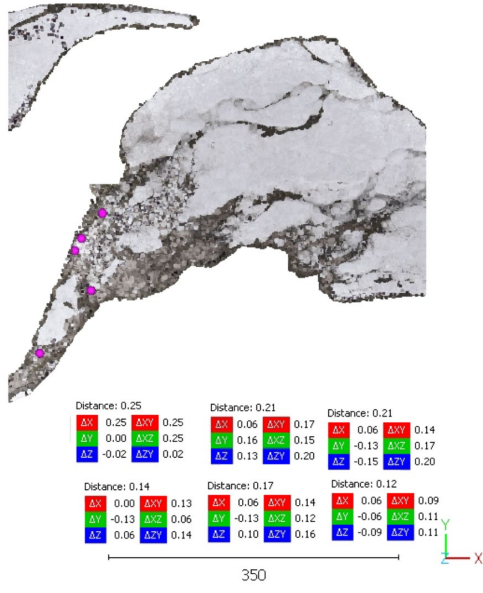
(d)

Figure 4.14 cont. Mapping of the ice jam at Niobrara River at Butte (Highway 11). (a) Position and the river water flow; (b) dense point cloud and the location of the parallel profiles; (c) dense point cloud and the location of the perpendicular profiles; (d) locations of the thickness measurement.

Table 4.9 Manning's n estimation for various section lengths at Niobrara River at Butte (Highway 11).

Profile region	Direction	Metrics	L= 0.3 m	L = 1 m	L = 3 m	L = 5 m	L = 10 m	L = 20 m
1_1	Para	IQR	0.0000	0.0003	0.0207	0.0223	0.0247	0.0278
		SD	0.0003	0.0155	0.0202	0.0220	0.0238	0.0276
		Mode	0.0000	0.0000	0.0000	0.0271	0.0287	0.0345
1_1	Perp	IQR	0.0003	0.0004	0.0210	0.0224	0.0258	0.0292
		SD	0.0003	0.0177	0.0213	0.0224	0.0249	0.0279
		Mode	0.0000	0.0000	0.0257	0.0273	0.0299	0.0334
1_2	Perp	IQR	0.0000	0.0003	0.0219	0.0232	0.0257	0.0289
		SD	0.0003	0.0168	0.0214	0.0237	0.0259	0.0283
		Mode	0.0000	0.0000	0.0266	0.0289	0.0313	0.0345
2_1	Para	IQR	0.0003	0.0004	0.0199	0.0220	0.0251	0.0277
		SD	0.0003	0.0156	0.0217	0.0232	0.0249	0.0260
		Mode	0.0000	0.0000	0.0285	0.0306	0.0303	0.0294
2_2	Para	IQR	0.0000	0.0004	0.0209	0.0225	0.0258	0.0279
		SD	0.0003	0.0167	0.0215	0.0226	0.0251	0.0278
		Mode	0.0000	0.0000	0.0279	0.0266	0.0316	0.0335
2_1	Perp	IQR	0.0003	0.0003	0.0186	0.0212	0.0234	0.0259
		SD	0.0003	0.0124	0.0183	0.0205	0.0230	0.0245
		Mode	0.0000	0.0000	0.0214	0.0242	0.0277	0.0283
2_2	Perp	IQR	0.0000	0.0003	0.0200	0.0211	0.0237	0.0264
		SD	0.0003	0.0156	0.0200	0.0219	0.0244	0.0265
		Mode	0.0000	0.0003	0.0256	0.0272	0.0298	0.0323
2_3	Perp	IQR	0.0003	0.0003	0.0209	0.0229	0.0250	0.0285
		SD	0.0003	0.0156	0.0213	0.0235	0.0249	0.0272
		Mode	0.0000	0.0000	0.0184	0.0291	0.0311	0.0342
3_1	Para	IQR	0.0000	0.0003	0.0194	0.0202	0.0225	0.0252
		SD	0.0003	0.0146	0.0196	0.0211	0.0232	0.0259
		Mode	0.0000	0.0000	0.0171	0.0289	0.0291	0.0324
3_2	Para	IQR	0.0000	0.0003	0.0186	0.0203	0.0229	0.0250
		SD	0.0003	0.0126	0.0184	0.0202	0.0227	0.0247
		Mode	0.0000	0.0000	0.0139	0.0271	0.0280	0.0303
3_1	Perp	IQR	0.0000	0.0004	0.0201	0.0218	0.0247	0.0273
		SD	0.0003	0.0169	0.0206	0.0218	0.0248	0.0275
		Mode	0.0000	0.0000	0.0003	0.0280	0.0307	0.0340

3_2	Perp	IQR	0.0000	0.0003	0.0199	0.0214	0.0244	0.0274
		SD	0.0003	0.0170	0.0208	0.0219	0.0246	0.0266
		Mode	0.0000	0.0000	0.0305	0.0295	0.0321	0.0324
4_1	Para	IQR	0.0000	0.0003	0.0219	0.0237	0.0263	0.0291
		SD	0.0003	0.0208	0.0243	0.0258	0.0271	0.0291
		Mode	0.0000	0.0000	0.0000	0.0003	0.0343	0.0376
4_2	Para	IQR	0.0000	0.0003	0.0235	0.0261	0.0277	0.0298
		SD	0.0003	0.0249	0.0281	0.0291	0.0301	0.0311
		Mode	0.0000	0.0000	0.0000	0.0000	0.0405	0.0423
4_3	Para	IQR	0.0000	0.0003	0.0202	0.0213	0.0248	0.0276
		SD	0.0003	0.0152	0.0207	0.0222	0.0258	0.0276
		Mode	0.0000	0.0000	0.0293	0.0301	0.0337	0.0356
4_1	Perp	IQR	0.0000	0.0004	0.0271	0.0288	0.0305	0.0320
		SD	0.0003	0.0236	0.0272	0.0286	0.0295	0.0312
		Mode	0.0000	0.0000	0.0331	0.0366	0.0362	0.0364
4_2	Perp	IQR	0.0003	0.0003	0.0213	0.0233	0.0269	0.0302
		SD	0.0149	0.0188	0.0232	0.0257	0.0277	0.0301
		Mode	0.0000	0.0000	0.0000	0.0000	0.0381	0.0407
4_3	Perp	IQR	0.0003	0.0003	0.0213	0.0233	0.0269	0.0302
		SD	0.0149	0.0188	0.0232	0.0257	0.0277	0.0301
		Mode	0.0000	0.0000	0.0000	0.0000	0.0381	0.0407
5_1	Para	IQR	0.0003	0.0004	0.0205	0.0229	0.0251	0.0273
		SD	0.0003	0.0172	0.0213	0.0235	0.0264	0.0284
		Mode	0.0000	0.0000	0.0265	0.0299	0.0338	0.0354
5_2	Para	IQR	0.0000	0.0003	0.0214	0.0234	0.0267	0.0291
		SD	0.0003	0.0188	0.0231	0.0239	0.0268	0.0284
		Mode	0.0000	0.0000	0.0291	0.0304	0.0325	0.0338
5_3	Para	IQR	0.0003	0.0004	0.0223	0.0255	0.0286	0.0313
		SD	0.0003	0.0202	0.0237	0.0260	0.0292	0.0315
		Mode	0.0000	0.0000	0.0315	0.0330	0.0371	0.0374
5_4	Para	IQR	0.0000	0.0003	0.0214	0.0237	0.0265	0.0295
		SD	0.0003	0.0174	0.0249	0.0262	0.0268	0.0300
		Mode	0.0000	0.0000	0.0003	0.0336	0.0336	0.0360
5_1	Perp	IQR	0.0000	0.0003	0.0186	0.0208	0.0237	0.0260
		SD	0.0003	0.0142	0.0215	0.0244	0.0252	0.0269
		Mode	0.0000	0.0000	0.0292	0.0348	0.0348	0.0375
5_2	Perp	IQR	0.0003	0.0004	0.0223	0.0235	0.0278	0.0311
		SD	0.0003	0.0202	0.0237	0.0250	0.0278	0.0300
		Mode	0.0000	0.0000	0.0321	0.0323	0.0326	0.0351

5_3	Perp	IQR	0.0000	0.0003	0.0223	0.0238	0.0259	0.0280
		SD	0.0003	0.0180	0.0224	0.0245	0.0264	0.0292
		Mode	0.0000	0.0000	0.0288	0.0191	0.0191	0.0191
5_4	Perp	IQR	0.0003	0.0004	0.0245	0.0269	0.0307	0.0323
		SD	0.0003	0.0209	0.0249	0.0268	0.0298	0.0306
		Mode	0.0000	0.0003	0.0315	0.0332	0.0364	0.0371

Table 4.10 Manning's n estimation for various section lengths at Loop River at Fullerton

Profile region	Direction	Metrics	L= 0.3 m	L = 1 m	L = 3 m	L = 5 m	L = 10 m	L = 20 m
1_1	Para	IQR	0.0003	0.0004	0.0179	0.0191	0.0205	0.0216
		SD	0.0003	0.0151	0.0203	0.0222	0.0230	0.0244
		Mode	0.0000	0.0000	0.0003	0.0003	0.0003	0.0003
1_2	Para	IQR	0.0003	0.0004	0.0193	0.0203	0.0226	0.0246
		SD	0.0003	0.0151	0.0187	0.0203	0.0227	0.0241
		Mode	0.0000	0.0000	0.0223	0.0247	0.0285	0.0294
1_1	Perp	IQR	0.0000	0.0004	0.0202	0.0217	0.0239	0.0264
		SD	0.0003	0.0241	0.0278	0.0291	0.0295	0.0316
		Mode	0.0000	0.0000	0.0378	0.0381	0.0379	0.0403
1_2	Perp	IQR	0.0003	0.0004	0.0177	0.0186	0.0195	0.0219
		SD	0.0003	0.0157	0.0190	0.0202	0.0207	0.0224
		Mode	0.0000	0.0000	0.0259	0.0266	0.0270	0.0301
2_1	Para	IQR	0.0000	0.0003	0.0185	0.0197	0.0210	0.0224
		SD	0.0003	0.0172	0.0202	0.0210	0.0223	0.0236
		Mode	0.0000	0.0000	0.0167	0.0302	0.0331	0.0331
2_1	Perp	IQR	0.0003	0.0149	0.0217	0.0223	0.0272	0.0288
		SD	0.0003	0.0171	0.0228	0.0221	0.0260	0.0271
		Mode	0.0000	0.0000	0.0297	0.0292	0.0322	0.0320
2_2	Perp	IQR	0.0000	0.0004	0.0189	0.0201	0.0221	0.0233
		SD	0.0003	0.0163	0.0195	0.0200	0.0221	0.0228
		Mode	0.0000	0.0003	0.0252	0.0253	0.0290	0.0292
2_3	Perp	IQR	0.0003	0.0127	0.0181	0.0197	0.0217	0.0237
		SD	0.0003	0.0158	0.0188	0.0194	0.0210	0.0222
		Mode	0.0000	0.0000	0.0230	0.0234	0.0257	0.0255
3_1	Para	IQR	0.0003	0.0004	0.0204	0.0224	0.0250	0.0264
		SD	0.0003	0.0182	0.0225	0.0240	0.0266	0.0291
		Mode	0.0000	0.0000	0.0289	0.0297	0.0332	0.0343
3_2	Perp	IQR	0.0000	0.0151	0.0253	0.0264	0.0314	0.0349
		SD	0.0003	0.0209	0.0258	0.0268	0.0307	0.0327
		Mode	0.0000	0.0000	0.0315	0.0314	0.0358	0.0368

Table 4.11 Manning's n estimation for various section lengths at Loop River at St. Paul.

Profile region	Direction	Metrics	L= 0.3 m	L = 1 m	L = 3 m	L = 5 m	L = 10 m	L = 20 m
1_1	Para	IQR	0	0.0157	0.0189	0.0193	0.0209	0.0222
		SD	0.0003	0.0162	0.0185	0.0190	0.0203	0.0216
		Mode	0	0	0	0.0227	0.0245	0.0252
1_2	Para	IQR	0	0.0141	0.0208	0.0222	0.0232	0.0243
		SD	0.0003	0.0187	0.0222	0.0234	0.0249	0.0258
		Mode	0	0	0	0.0302	0.0314	0.0340
1_1	Perp	IQR	0	0.0146	0.0207	0.0219	0.0232	0.0250
		SD	0.0003	0.0167	0.0210	0.0230	0.0235	0.0260
		Mode	0	0	0.0262	0.0292	0.0292	0.0308
1_2	Perp	IQR	0	0.0170	0.0219	0.0237	0.0250	0.0283
		SD	0.0003	0.0199	0.0225	0.0241	0.0250	0.0267
		Mode	0	0	0.0285	0.0301	0.0301	0.0304
2_1	Para	IQR	0	0.0160	0.0225	0.0237	0.0258	0.0270
		SD	0.0003	0.0220	0.0259	0.0272	0.0280	0.0289
		Mode	0	0	0	0.0374	0.0382	0.0362
2_1	Perp	IQR	0	0.0167	0.0236	0.0253	0.0261	0.0271
		SD	0.0003	0.0218	0.0248	0.0254	0.0264	0.0269
		Mode	0	0	0.0321	0.0330	0.0330	0.0318
3_1	Para	IQR	0.0003	0.0145	0.0195	0.0204	0.0222	0.0228
		SD	0.0160	0.0207	0.0225	0.0230	0.0236	0.0243
		Mode	0	0	0	0.0328	0.0331	0.0345
3_1	Perp	IQR	0.0003	0.0155	0.0204	0.0215	0.0231	0.0249
		SD	0.0003	0.0188	0.0220	0.0235	0.0253	0.0261
		Mode	0	0	0.0286	0.0297	0.0332	0.0329
3_2	Perp	IQR	0.0003	0.0160	0.0207	0.0217	0.0239	0.0244
		SD	0.0003	0.0189	0.0217	0.0227	0.0237	0.0245
		Mode	0	0.0003	0.0279	0.0003	0.0003	0.0003

Table 4.12 Manning's n estimation for various section lengths at Missouri River at Omaha.

Profile region	Direction	Metrics	L= 0.3 m	L = 1 m	L = 3 m	L = 5 m	L = 10 m	L = 20 m
1_1	Para	IQR	0	0.0003	0.0204	0.0213	0.0229	0.0244
1_1	Para	SD	0.0157	0.0204	0.0235	0.0252	0.0267	0.0301
1_1	Para	Mode	0	0	0.0351	0.0389	0.0383	0.0413
1_1	Perp	IQR	0	0.0003	0.0216	0.0237	0.0242	0.0258
1_1	Perp	SD	0.0003	0.0213	0.0239	0.0254	0.0261	0.0266
1_1	Perp	Mode	0	0	0.0168	0.0320	0.0324	0.0324
1_2	Perp	IQR	0	0.0003	0.0221	0.0229	0.0245	0.0260
1_2	Perp	SD	0.0003	0.0205	0.0236	0.0253	0.0284	0.0310
1_2	Perp	Mode	0	0	0.0314	0.0339	0.0380	0.0377
1_3	Perp	IQR	0	0.0003	0.0208	0.0216	0.0232	0.0255
1_3	Perp	SD	0.0003	0.0198	0.0248	0.0256	0.0293	0.0312
1_3	Perp	Mode	0	0	0.0357	0.0354	0.0395	0.0398
2_1	Para	IQR	0	0	0.0202	0.0219	0.0237	0.0245
2_1	Para	SD	0.0003	0.0183	0.0230	0.0245	0.0256	0.0260
2_1	Para	Mode	0	0	0.0157	0.0342	0.0359	0.0345
2_1	Perp	IQR	0	0.0003	0.0214	0.0228	0.0243	0.0250
2_1	Perp	SD	0.0003	0.0188	0.0228	0.0244	0.0254	0.0260
2_1	Perp	Mode	0	0	0.0281	0.0307	0.0324	0.0342
2_2	Perp	IQR	0	0.0003	0.0202	0.0219	0.0229	0.0236
2_2	Perp	SD	0.0003	0.0176	0.0208	0.0226	0.0238	0.0243
2_2	Perp	Mode	0	0	0.0256	0.0291	0.0276	0.0279
3_1	Para	IQR	0	0.0003	0.0218	0.0224	0.0234	0.0247
3_1	Para	SD	0.0003	0.0204	0.0245	0.0258	0.0262	0.0284
3_1	Para	Mode	0	0	0.0343	0.0360	0.0360	0.0351
3_1	Perp	IQR	0	0.0003	0.0218	0.0224	0.0234	0.0247
3_1	Perp	SD	0.0003	0.0204	0.0245	0.0258	0.0262	0.0284
3_1	Perp	Mode	0	0	0.0343	0.0360	0.0360	0.0351
3_2	Perp	IQR	0	0.0003	0.0222	0.0235	0.0252	0.0258
3_2	Perp	SD	0.0168	0.0239	0.0271	0.0274	0.0299	0.0318
3_2	Perp	Mode	0	0	0.0374	0.0371	0.0393	0.0401
4_1	Para	IQR	0	0.0003	0.0208	0.0218	0.0231	0.0243
4_1	Para	SD	0.0178	0.0210	0.0235	0.0246	0.0257	0.0272
4_1	Para	Mode	0	0	0.0355	0.0356	0.0342	0.0359
4_2	Para	IQR	0	0.0003	0.0198	0.0210	0.0224	0.0233

		SD	0.0003	0.0176	0.0204	0.0214	0.0223	0.0230
		Mode	0	0	0	0.0285	0.0277	0.0281
4_1	Perp	IQR	0	0.0004	0.0208	0.0218	0.0232	0.0249
		SD	0.0003	0.0247	0.0273	0.0301	0.0316	0.0325
		Mode	0	0	0.0378	0.0416	0.0418	0.0404
4_2	Perp	IQR	0	0.0111	0.0233	0.0250	0.0266	0.0284
		SD	0.0003	0.0241	0.0271	0.0273	0.0314	0.0341
		Mode	0	0	0.0355	0.0345	0.0409	0.0412
4_3	Perp	IQR	0	0.0003	0.0213	0.0223	0.0226	0.0249
		SD	0.0003	0.0201	0.0242	0.0258	0.0272	0.0298
		Mode	0	0	0	0.0361	0.0361	0.0394
5_1	Para	IQR	0	0.0003	0.0186	0.0198	0.0211	0.0218
		SD	0.0003	0.0152	0.0195	0.0208	0.0219	0.0229
		Mode	0	0	0.0274	0.0293	0.0285	0.0282
5_1	Perp	IQR	0	0.0003	0.0197	0.0212	0.0223	0.0239
		SD	0.0003	0.0180	0.0212	0.0217	0.0230	0.0268
		Mode	0	0	0.0257	0.0270	0.0290	0.0332

4.6 Chapter Summary

In this chapter, two methods for estimating Manning's n, a critical parameter in hydraulic modeling, were applied to ice thickness data collected from various river sites. The first method utilized the Nazikhovskiy equation, while the second method involved statistical analysis of UAS-derived data, focusing on residuals from ice thickness profiles. Both approaches yielded consistent results, with the standard deviation and other statistical measures aligning closely between the two methods. For instance, for the Niobrara River at the Highway 281 site, the median ice thickness was 0.13 meters, corresponding to a Manning's n value of 0.019. Similarly, at the Loop River in Fullerton, a median thickness of 0.24 meters was associated with a Manning's n value of 0.031. This consistency across methods suggests both are reliable for estimating Manning's n in river ice conditions.

Given the simplicity and reliability of the results derived from thickness measurements alone, it is recommended that these values be used directly in hydraulic models. The range of median ice thickness values, from 0.13 meters at the Niobrara Highway 281 to 0.24 meters at Loop River in Fullerton, and the corresponding Manning's n values, from 0.019 to 0.031, provide a straightforward and accurate basis for modeling, as summarized in Table 4.6. Using these thickness-derived values will simplify the modeling process while maintaining the necessary accuracy for predicting and managing ice-related challenges in river systems.

Chapter 5 Hydraulic Modeling

5.1 Overview Modeling

Ice shear is not built into the HEC-RAS 2D software. However, it can be modeled by adjusting the bed shear appropriately. The bed shear stress, τ_b, can be used to absorb the ice shear through implementation of an adjusted Manning's n value. Although the ice influences the top surface of the water column and bed shear stresses occur on the bottom surface, applying ice effects at the bottom has no impact in a depth-averaged model because vertical variations are all averaged. In addition, it may also be useful to make an adjustment to mix coefficients that account for changes in the velocity distribution, but this was not considered in this case study analysis.

Since the shallow water equations are depth-averaged, one can use the bed shear stress term to represent flow resistance anywhere in the water column. The formation of an ice layer has multiple impacts on these shear stresses. Based on Equation 2.13: (1) the flow area is reduced because the weight of the ice pushes it down into the flow, (2) the wetted perimeter of the flow is increased because there is now a stationary boundary on both the upper and lower surfaces of the flow, and (3) the compound roughness of the flow is different from the roughness without ice.

Reduction in flow area has two effects. First, it reduces the hydraulic radius of the flow, and second, it increases the velocity for the same flow rate. Both changes increase the effective shear stress in Equation 2.13. Moreover, the increase in wetted perimeter also reduces the hydraulic radius of the flow, causing an increase in the effective shear stress as long as the ice layer is stationary. An increase in the compound roughness of the combined ice layer and bed of the river would result from ice break-up followed by jamming. One can assume, at least initially,

that the roughness in the air and underwater is similar when a jam first occurs. UAS measurements provide an estimate of the roughness above the ice. Of course, over time, the roughness below the jam would likely decrease due to melting and refreezing, but the initial roughness may be the same on both sides of the ice layer.

This chapter demonstrates the impacts of a rough ice cover by representing all impacts, reduced flow area, increased wetted perimeter, and increased composite Manning's roughness. A rough ice cover also increases the overall Manning's roughness of the flow in the main channel. This includes two cases: first, the modeled flooding caused by observed flows if there is no ice layer, and second, how the presence of an ice layer impacts the flooding.

5.2 Model Description

The focus of the hydraulic modeling effort is the Loup River near Columbus. The site selected is particularly susceptible to ice jams and was subject to massive ice flows during the 2019 flood. Additional ice jamming occurred in 2022, although the team did not have access to the site during the ice jam.

Figure 5.1 is an aerial ortho-projected view of the site. At the top of the site is Lake Oconee, a small lakeside community near Columbus. The houses in this community have not experienced flooding due to ice jams, but in 2022 the water nearly reached the crown of the road around the community during the breakup of an ice jam. The land south of the river is agricultural with some forested areas. A digital elevation model (DEM) of the study site shown in Figure 5.2 shows that large areas of the floodplain are susceptible to flooding. It is fascinating to observe DEMs of alluvial rivers such as the Loup because preferential flow paths sculpted by past floods are clearly visible. The team selected the meshing area based on the DEM and the areas that were likely to be flooded in the case of extreme flows.

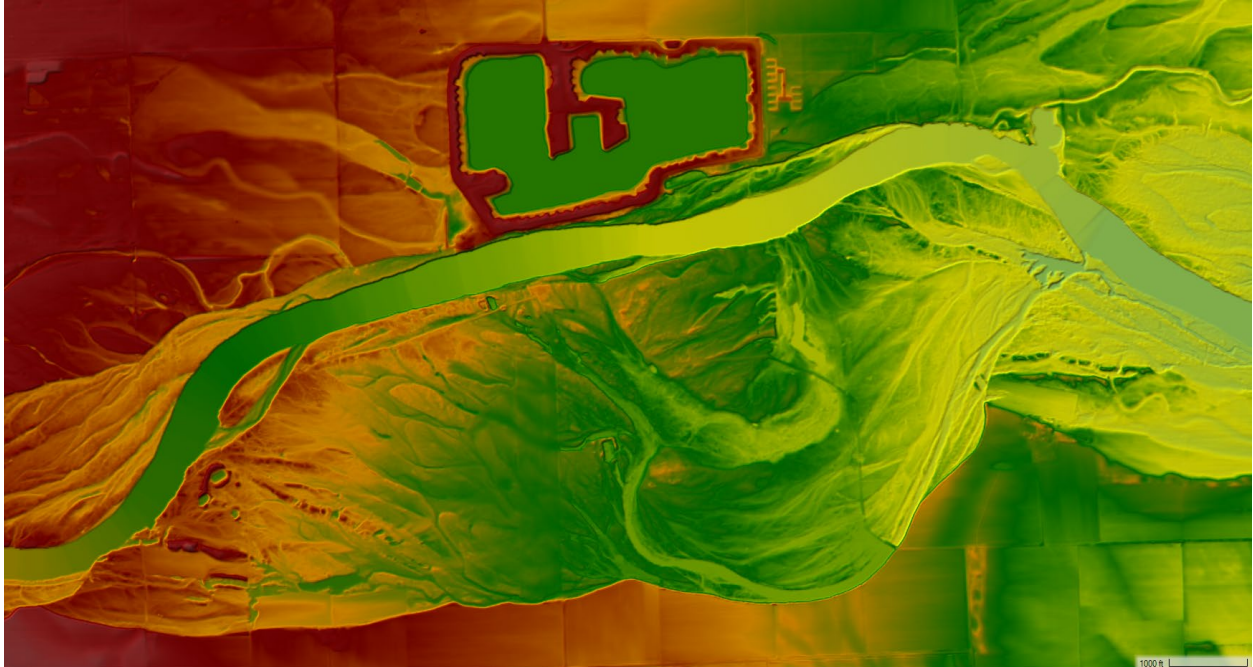Figure 5.1 Aerial orthomosaic image of the study site.

Figure 5.2 DEM of the study site.

5.2.1 Hydraulic Modeling Parameters

The team applied a high-resolution 2D mesh to the study site as shown in Figure 5.3. The mesh grid cells are 6 m × 6 m (20 ft × 20 ft) in the main channel and 15.2 m × 15.2 m (50 ft × 50 ft) in the floodplain, with variations in shape at the break lines and near the thalweg. The overall length of the study reach was about five kilometers (17,000 ft) along the channel centerline.

Figure 5.3 HEC-RAS 2D model extents.

A map of Manning's roughness conditions used for the model are shown in Figure 5.4. Model roughness varies from 0.02 to 0.10 with a main channel roughness of 0.02. The main channel roughness used by the model was selected based on other studies on the Platte River, a nearby river with similar characteristics. The Platte and Loup Rivers are both wide, shallow sand-bed rivers. FEMA (2007) suggested that the main channel roughness of the lower Platte

River is between 0.017 and 0.025. Similarly, Randle and Samad (2008) used a Manning's roughness of 0.024 for the central Platte River. Floodplain roughness for the current model ranged up to 0.10, depending on cover type, and land cover was assessed from maps and aerial imagery.
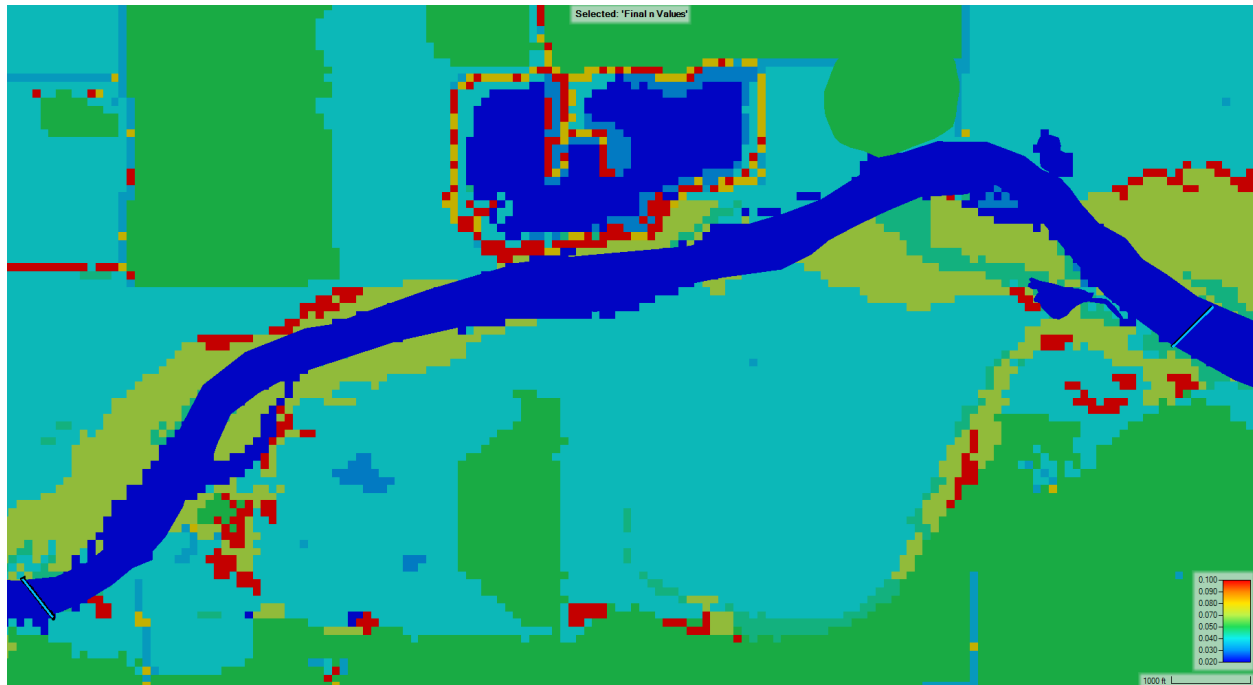

Figure 5.4 Manning's Roughness of the main channel and floodplain.

For the upstream boundary condition, the team applied the hydrograph shown in Figure 5.5. These are the flow records for the Loup River for the 2019 flood obtained from a USGS stream gauge (06793000) located upstream of the study site. The simulated period was from the start of March 13, 2019, to the end of March 15, 2019. The peak flow rate shown in Figure 5.5 is about 3300 m^3/s (120,000 ft^3/s) which is one of the highest flow rates on record. The flow rate ramps up from 100 m^3/s very quickly and peaks very early in the morning on March 14. The team used a normal depth boundary condition at the outlet. A warmup time of 24 hours was

applied to the model to ensure the model was filled and at steady state as soon as the hydrograph began Computation intervals were 30 seconds and hydrograph data were stored every 10 minutes.
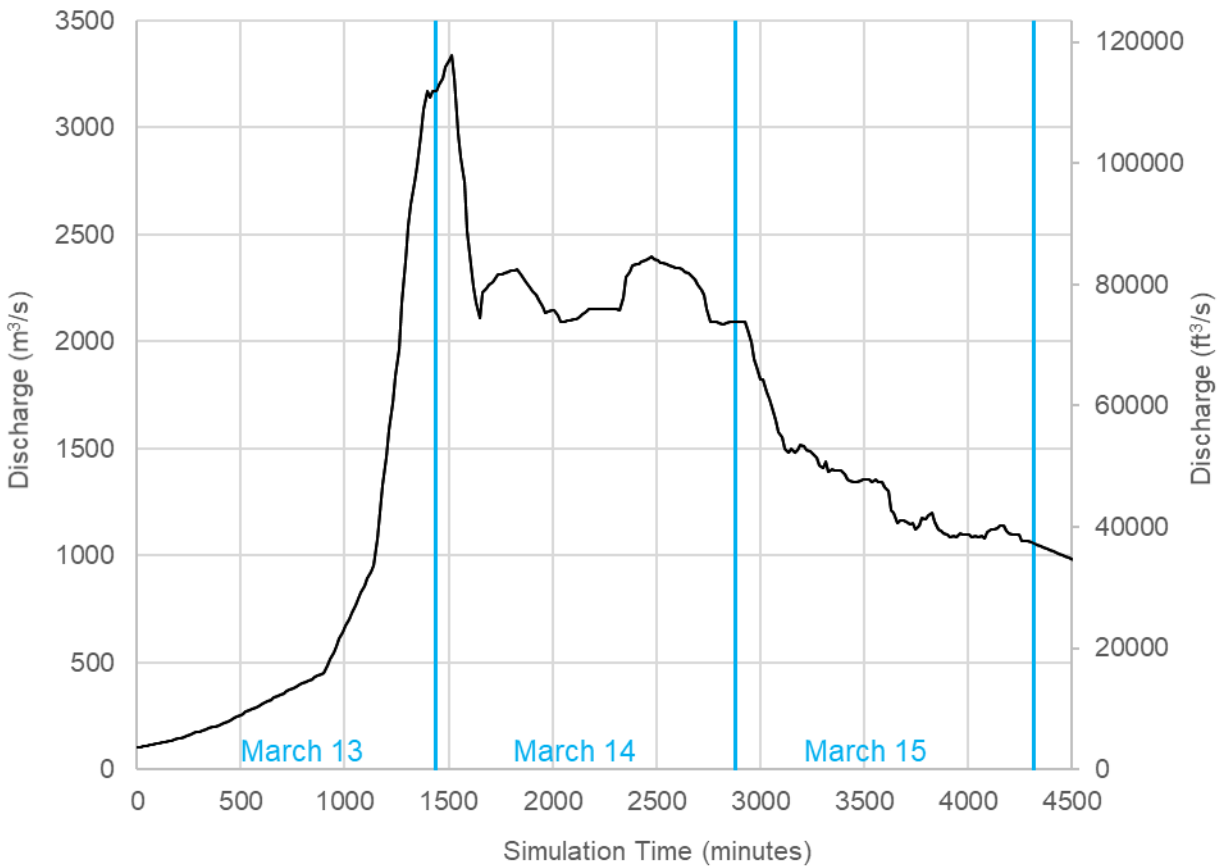

Figure 5.5 Simulated hydrograph for the Loup River.

5.2.2 Results

The model results are shown in Figure 5.6. These results show what the flooding is when ice is not considered in the calculations because the roughness of the main channel was chosen to be 0.02. Even without the presence of ice, the flood is far greater than what the main channel can

handle In fact, water begins to enter the floodplain at about 3:00 PM on March 13, when the flow is only 450 m³/s (16,000 ft³/s). The peak flow is roughly seven times that amount.
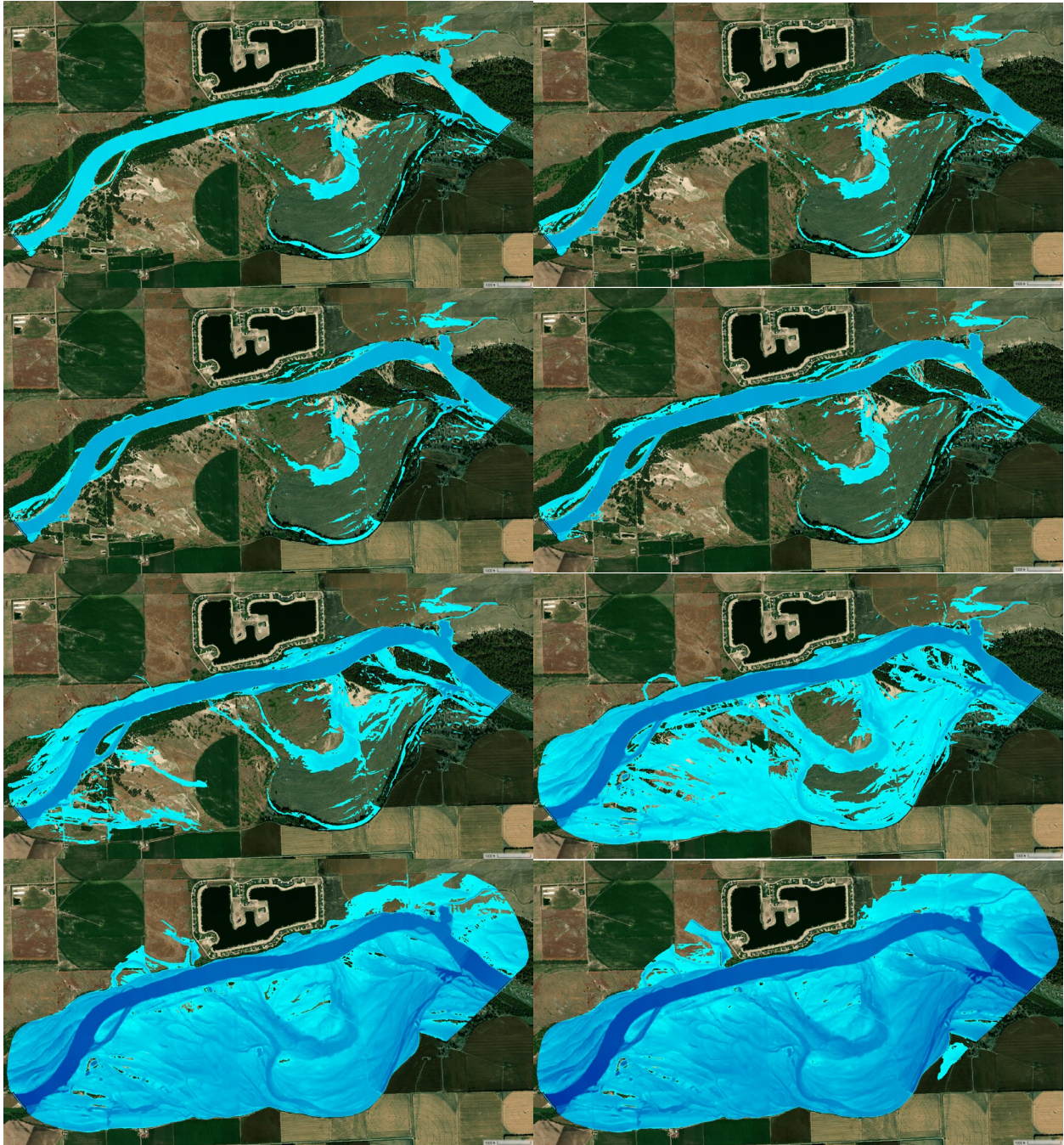

Figure 5.6 Time sequence of flow depths for a main channel roughness of 0.02. Times are for March 13 at (a) 12:00 AM., (b) 12:00 PM, (c) 2:00 PM., (d) 4:00 PM, (e) 6:00 PM, (f) 8:00 PM, (g) 10:00 PM., and (h) 12:00 AM of March 14.

However, from our measurements of ice roughness done using the UAS, the team estimates the roughness in the main channel can be as much as 0.04 (Chapter 4) if broken ice is the source of the roughness. When this roughness is used in the main channel of the model, the following results are obtained and shown in Figure 5.7. The main assumption here is that the ice is not moving, but that it crumples and increases the overall roughness of the main channel and that the increase in the roughness can be asserted based on our literature review and on the observations made from UAS measurements. For the increased roughness, water begins to enter the floodplain at about 8:00 AM on March 13. This occurs at a flow rate of 245 m^3/s (8700 ft^3/s), which is roughly half the flow rate of the previous case, when the main channel roughness was 0.02.

In fact, the rain on snow event of March 13 was so large that flooding was extreme even without the effects of ice. Nevertheless, the presence of the ice exacerbates the flooding and will lead to flooding for significantly lower flow rates.

Figures 5.8 and 5.9 show a model run and the aerial image of a channel cut-off in the study area. The images show where the flow bypasses a corner when it is backed up due to a constriction in the channel. This constriction is likely a location where ice jamming occurs. A closeup of the outlet of this cut-off in Figure 5.10 demonstrates the erosion that can occur when ice jamming and subsequent bypassing of the flow through the floodplain occurs. The type of head-cutting shown in Figure 5.10 can lead to permanent cut-off channels.
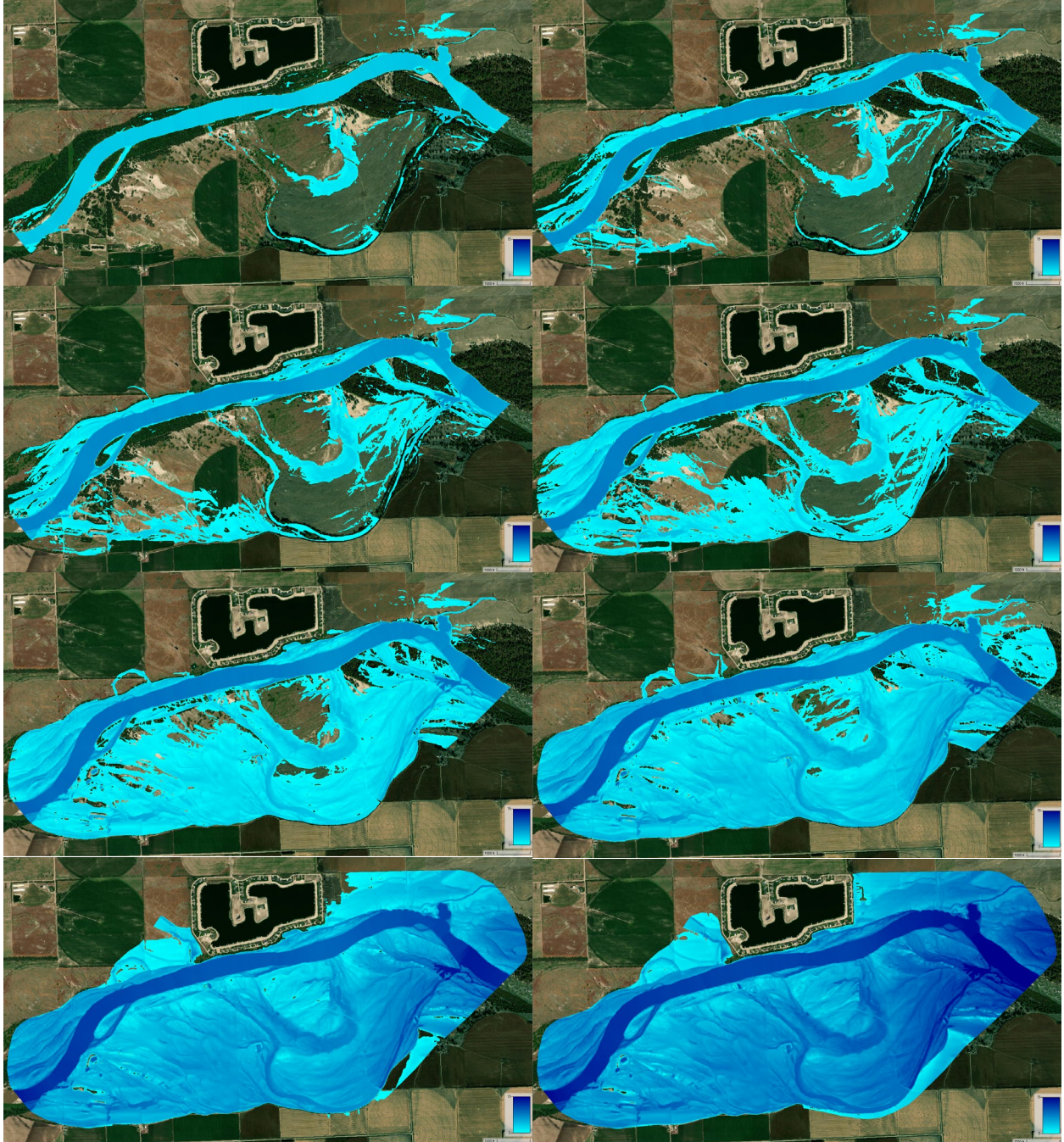
Figure 5.7 Time sequence of flow depths for a main channel roughness of 0.04. Times are for March 13 at (a) 12:00 AM, (b) 12:00 PM, (c) 2:00 PM, (d) 4:00 PM, (e) 6:00 PM, (f) 8:00 PM, (g) 10:00 PM, and (h) 12:00 AM of March 14.
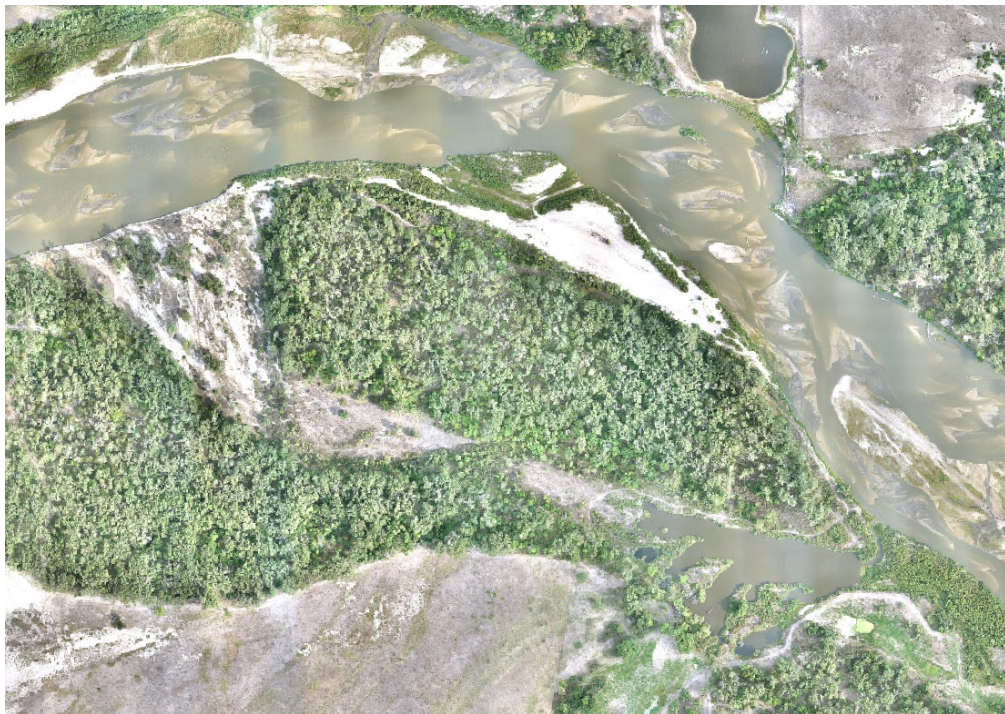
Figure 5.8 Close-up of a channel cutoff.

Figure 5.9 Aerial Image of Loup channel cutoff.

Figure 5.10 Close up of a head-cut caused by the cut-off.

5.3 Chapter Summary

In this chapter, a simple demonstration was provided on how increases in roughness due to ice can increase flooding. It was shown that the increases in Manning's roughness caused by ice covers can significantly increase water depths for the same flows. The team measured roughness using UAS measurements over a typical rubble pile and estimated the roughness to be about 0.04. When this roughness was introduced to the main channel of one of our test sites, the project found that flooding occurred at about half the flow rates than for a channel unaffected by ice. No adjustments were made to Manning's roughness within the floodplain, but it is likely that if large quantities of ice are present, it will also reduce the conveyance capacity of the floodplain. The project also observed that ice jamming can lead to the formation of cutoffs. A temporary cutoff was observed in the present case, but a more permanent one could easily form with additional head-cut erosion at the downstream end of the cutoff.

Chapter 6 Conclusions

6.1 Overview Conclusions

The research presented in this study provides a comprehensive understanding of ice jams and their impact on river systems in Nebraska, highlighting the unique challenges posed by the state's fluvial geomorphology. Through the development of a two-dimensional hydrodynamic model, the study offers new insights into the behavior of ice flows and jams in rivers with high sediment loads, steep gradients, and wide conveyance areas. The model, which integrates hydrological data, digital elevation models (DEM) from UAS surveys, and platforms like HEC-RAS 2D and QGIS, has demonstrated its potential to accurately simulate the complex dynamics of ice jams, including their effects on river morphology and infrastructure.

One of the key findings of this research is the significant influence of ice flows on the morphology of Nebraska's rivers. The study's data, collected through extensive UAS surveys and field measurements, reveal that ice jams can substantially alter floodplain characteristics and cause damage to critical infrastructure such as bridges and low-head dams. These findings underscore the importance of considering ice-related hazards in the design and management of infrastructure in regions prone to such events. The research also highlights the limitations of existing one-dimensional models, and the advantages of the two-dimensional approach adopted in this study, which offers a more detailed and accurate representation of ice dynamics in complex river systems.

Moreover, the study's methodology, which includes the use of UASs for high-resolution data collection and the application of advanced statistical techniques for analyzing ice thickness and roughness, represents a significant advancement in the field of hydraulic modeling. The research demonstrates that UAS technology, combined with robust data processing and analysis

methods, can provide detailed and reliable data for modeling ice-related processes. This approach not only enhances the accuracy of the models but also offers a safer and more efficient alternative to traditional survey methods.

HEC-RAS 2D serves as a widely utilized tool in hydraulics, operating on the principles of the Shallow Water Equations. The model can be extended to incorporate ice cover by adjusting Manning's roughness and utilizing the Manning-Strickler representation of shear stress. By increasing the roughness in a 2D model of a specific study site, the team modified Manning's roughness to reflect the roughness extrapolated for an ice rubble pile, demonstrating that an ice layer can significantly increase flooding for identical flow rates.

In conclusion, this study contributes valuable knowledge to the field of river ice dynamics, particularly in the context of unique geomorphological settings like those found in Nebraska. The findings have practical implications for infrastructure design and flood risk management, providing engineers and planners with the tools and data needed to address the challenges posed by ice jams. The research also opens avenues for further studies, particularly in refining the two-dimensional hydrodynamic model and exploring its application in other regions with similar fluvial characteristics. As climate change continues to influence weather patterns and river behavior, the importance of understanding and mitigating ice-related hazards will only grow, making the contributions of this study both timely and critical.

6.2 Future Work to Consider

Future work should include expanding the study to more ice jam sites across Nebraska and other regions to enhance the robustness and applicability of the two-dimensional hydrodynamic model. Additionally, efforts should be made to develop methods for underwater assessments of ice jams, which are currently limited due to equipment constraints and safety

concerns. Experimentation is also needed to verify the UAS-derived values of Manning's

number, ensuring the accuracy of these critical parameters in hydraulic modeling. Finally, further

hydraulic modeling and validation are necessary to refine the model, improving its predictive

capabilities and applicability to a wider range of river conditions.

References

Aberle, J. and Nikora, V.: Statistical properties of armored gravel bed surfaces, Water Resour. Res., 42, W11414, https://doi.org/10.1029/2005WR004674, 2006.

ASDSO Association of State Dam Safety Officials (2020). Spencer Dam Failure Investigation Report. Investigative Panel Report by M. Baker, R. Ettema, M. Teal, and J. Trojanowski.

Ashton, G. D. (Ed.): River and lake ice engineering, Water Resources Publication, Chelsea, Michigan, USA, 261–361, ISBN 0-918334-59-4, 1986.

Beltaos S. Hydraulic roughness of breakup ice jams [J]. Journal of Hydraulic Engineering, ASCE, 2001, 127(8): 650-656.

Chow, V.T. (1959) Open-channel Hydraulics, McGraw-Hill Publishing, Boston, MA. 680 pp.

Dingman, S.L. (2009) Fluvial Hydraulics, Oxford University Press, 559 pp.

Ehrman, J., Clark, S., and Wall, A. (2021) "Ice roughness estimation via remotely piloted aircraft and photogrammetry," The Cryosphere, 15, pp. 4031-4046.

FEMA, Federal Emergency Management Agency (2007) Flood Insurance Study, Volume 1, Sarpy County, Nebraska and incorporated areas. Flood Insurance Study Number 31153CV001B. October, 2007.

Gibson, S. and Boyd, P. (2016) "Monitoring, measuring and modeling a reservoir flush on the Niobrara River in the Sandhills of Nebraska," River Flow 2016 – Proceedings of the International Conference on Fluvial Hydraulics, pp. 1448-1455.

Gomez, B.: Roughness of Stable, Armored Gravel Beds, Water Resour. Res., 29, 3631–3642, 1993.

Hicks, F. and Beltaos, S. (2008) "River Ice" in Cold Region Atmospheric and Hydrologic Studies, The Mackenzie GEWEX Experience, Vol 2. Ed. Ming-ko Woo. Springer-Verlaag, Berlin, pp. 281-306.

https://waterdata.usgs.gov/monitoring-location/06793000/#parameterCode=00065&period=P7Dhttps://csdms.colorado.edu/wiki/Model_download_portal

Manitoba Hydro (2022) CRISSP2D Programmer Manual V1.4, Originally developed for CEA Technologies Inc., 158 pp.

Mollenkamp, Allison (July 2, 2019). "Nebraska Roads and Bridges Still in Recovery After Flooding," netnebraska.org. NET Nebraska News.

Nikora, V. I., Goring, D. G., and Biggs, B. J. F.: On gravel-bed roughness characterization, Water Resour. Res., 34, 517–527, 1998.

Randle, T.J. and Samad, M.A. (2008) Platte River in Central Nebraska Modeling of Pulse-Flow Release, Technical Report No. SRH-2008-2, US Bureau of Reclamation.

Schwartz, Matthew (March 21, 2019). "Nebraska faces over $1.3 billion in flood losses," www.npr.org. Nebraska Public Media.

Shen, H.T., Liu, L.W., and Chen, Y.C. (2001) "River ice dynamics and ice jam modeling," IUTAM Symposium on Scaling Laws in Ice Mechanics and Ice Dynamics, Eds. J. Dempsey and H. Shen, Kluwer Academic Publishers, pp. 349-362.

Strickler, A. (1923). "Beiträge zur Frage der Geschwindigkeitsformel und der Rauhigkeitszahlen fur Ströme, Kanäle und Geschlossene Leitungen," (Some contributions to the problem of the velocity formula and roughness factors for rivers, canals, and closed conduits), Mitteilungen des eidgenössischen Amtes für Wasserwirtschaft, Bern, Switzerland, no. 16.

Sturm, T. (2010). Open Channel Hydraulics, McGraw-Hill Publishing, New York. 546 pp.

USGS (2022) https://apps.nationalmap.gov/ Website that provides Geographical Information Systems Data for the United States.

Vreugdenhil, J. (1994) Numerical methods for shallow water flow, Kluwer Academic Publishers, Dordrecht, Netherlands.